

The influence of near surface sediment hydrothermalism on the TEX₈₆ tetraether lipid-based proxy and a new correction for ocean bottom lipid overprinting

Jeremy N. Bentley ^a, Gregory T. Ventura ^a, Clifford C. Walters ^b, Stefan M. Sievert ^c, Jeffrey S. Seewald ^c

^a Department of Geology, Saint Mary's University, Halifax, Nova Scotia B3H 3C3, Canada.

^b Bureau of Economic Geology, University of Texas at Austin, USA.

^c Woods Hole Oceanographic Institution, Woods Hole, USA.

* Corresponding author: Todd.ventura@smu.ca

For submission to *Biogeosciences*

Number of pages: 27

Number of Figures: 6

Number of Tables: 2

Supplementary pages: 6

Key Points

- High *i*GDGTs turnover in shallow sediments is shown to be non-selective and does not impact TEX₈₆ paleoclimate ratios.
- The proxy can be overprinted by sediment sourced lipids when geothermal temperatures rise above ~60–70 °C.
- A universally applicable, diagenetic correction model is presented to remove overprinting artifacts in the TEX₈₆ proxy.

Abstract

The diversity and relative abundances of tetraether lipids produced by archaea and bacteria in soils and sediments are increasingly used to assess environmental change. For instance, the TetraEther index of 86 carbon atoms (TEX₈₆), based on archaeal isoprenoidal glycerol dialkyl glycerol tetraether (*i*GDGT) lipids, is frequently applied to reconstruct past sea-surface temperatures (SST). Yet, it is unknown how the ratio fully responds to environmental and/or geochemical variations and if the produced signals are largely the adaptive response by Thaumarchaeota to oceanographic effects associated with climate or seasonal temperature changes in the upper water column. We present the results of a four push-core transect study of surface sediments collected along an environmental gradient at the Cathedral Hill hydrothermal vent system in Guaymas Basin, Gulf of California. The transect crosses a region where advecting hydrothermal fluids reach 155 °C within the upper 21cm below the seafloor (cmbsf) close to the vent center to near ambient conditions at the vent periphery. The recovered *i*GDGTs closest to the vent center experienced high rates of turnover with up to 94% of the lipid pool being lost within the upper 21 cmbsf. Here, we show that the turnover is non-selective across TEX₈₆ GDGT lipids and does not affect the ratio independently. However, as evident by TEX₈₆ ratios being highly correlated to the Cathedral Hill vent sediment porewater temperatures ($R^2 = 0.84$), the ratio can be strongly impacted by the combination of severe lipid loss coupled with the addition of *in situ* *i*GDGT production from archaeal communities living in the vent sediments. The resulting overprint produces absolute temperature offsets of up to 4 °C based on the TEX₈₆^H-calibration relative to modern climate records of the region. The overprint is also striking given the flux of *i*GDGTs from the upper water column is estimated to be ~93% of the combined intact polar lipid (IPL) and core GDGT lipid pool initially deposited on the seafloor. A model to correct the overprint signal using IPLs is

therefore presented that can similarly be applied to all near-surface marine sediment systems where calibration models or climate reconstructions are made based on the TEX₈₆ measure.

1. Introduction

Archaeal and bacterial tetraether cellular membrane lipids represent a group of common and structurally diverse compounds frequently used to track the presence of living and dead microorganisms as well as geochemical and physical conditions within present-day and paleoenvironments (e.g., Schouten et al., 2002, 2004; 2013; Hopmans et al., 2004; Weijers et al., 2007, 2014; Hollis et al., 2012; O'Brien, et al., 2017; Stuart et al., 2017). In this regard, the proportional abundances of these lipids form various prominent proxies for assessing environmental change through time. For example, TEX₈₆ (TetraEther indeX with 86 carbon atoms; Schouten et al., 2002) is a widely used archaeal lipid-based paleotemperature proxy for marine environments. The ratio measures variations in the number of cyclopentyl rings for a select group of archaeal core lipids (CLs) (Supplementary Figure S1) following the assumption that biphytanyl cyclization is an organismal response to changing sea surface temperatures (SSTs). The proxy is therefore used in many regions around the world with TEX₈₆ values typically ranging from 0.2–0.9 in marine settings (e.g. Huguet et al., 2006; Kim et al., 2008; McClymont et al., 2012; Tierney, 2014). The utility of TEX₈₆ rests on the premise that *i*GDGTs found in ocean bottom sediments are almost exclusively produced by marine planktonic archaea that inhabit the epipelagic zone (Wakeham et al., 2003; Tierney, 2014; Besseling et al., 2019, 2020). Lipids are therefore required to be efficiently and continually transported from the upper water column to the underlying ocean floor to produce a fossil chemostratigraphic record of microbial response to changing SST conditions with time (Wuchter et al., 2005).

Since its introduction, the reliability of TEX₈₆ to accurately track paleoclimate variations has been questioned. TEX₈₆-based SST estimates have been observed to substantially deviate from other temperature proxies (e.g. Huguet et al., 2006; Rommerskirchen et al., 2011; Seki et al., 2012). For example, over the past decade, considerable effort has been made to reconstruct the early Paleogene greenhouse climate system. However, TEX₈₆ appears to significantly over-estimate reconstructed SSTs (Hollis et al., 2012) relative to other proxies such as Mg/Ca, or clumped isotopic compositions of foraminiferal calcite, as well as various climate models based on partial pressure of carbon dioxide ($p\text{CO}_2$) predictions (Lunt et al., 2012; Naafs et al., 2018). For late Neogene climate reconstructions, TEX₈₆ has been shown to underestimate warming trends relative to the U_{37}^{kl} alkenone-index (Brassell et al., 1986) derived temperatures (Lawrence et al., 2020). The apparent SST offsets have been attributed to how the proxy's associated lipids change in relation to their environment and if these changes are regulated by internal adaptations within the archaeon or by an overarching community succession. In this regard, the debate surrounding these discrepancies largely centers on establishing responses to seasonal biases (e.g. Herford et al., 2006; Wuchter et al., 2006; Huguet et al., 2011); the development of adequate calibration methods (e.g. Kim et al., 2010; Pearson et al., 2013; Tierney et al. 2014); identifying lipid sourcing effects – including subsurface sediments origins for those used with the calculation of TEX₈₆ (e.g. Lipp and Hinrichs, 2009); as well as physical, chemical, and ecological controls for archaeon *i*GDGTs cyclization (e.g. Elling et al., 2015; Qin et al., 2015; Hurley et al., 2016).

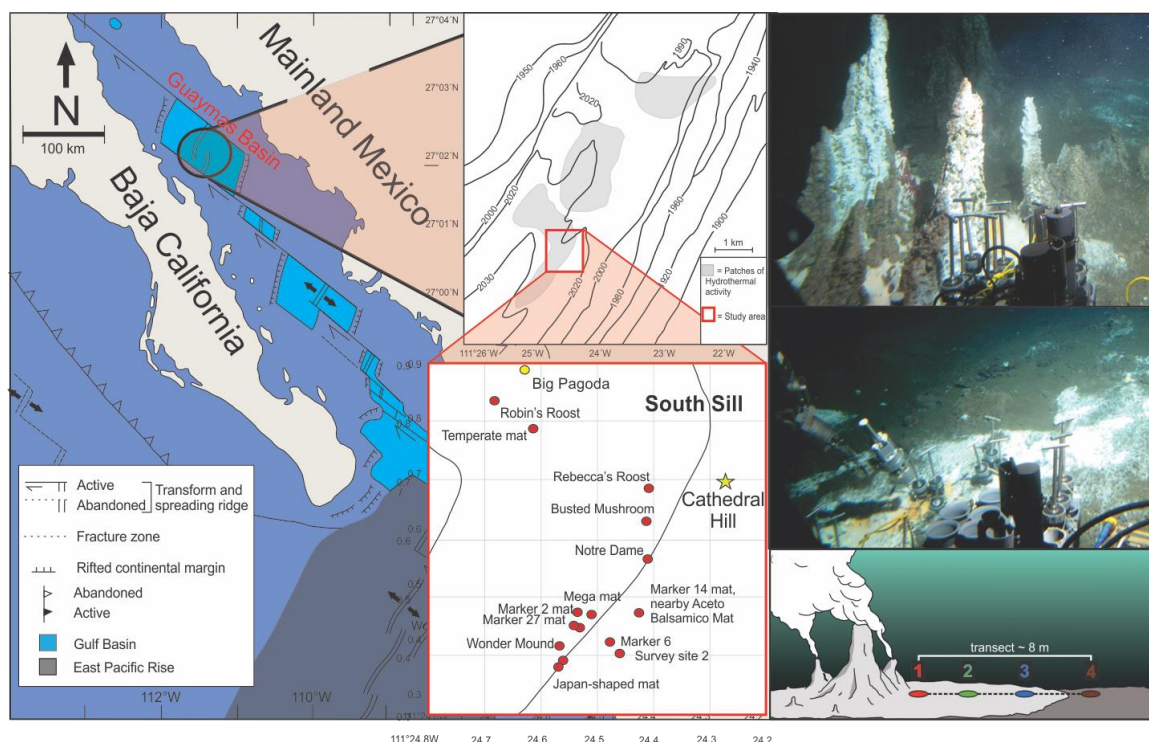
For non-thermal influences, the primary concern is what archaeal taxa produce *i*GDGTs and where they are sourced. To this end, most TEX₈₆ lipids are thought to be produced by Marine Group I (MGI) planktonic Thaumarchaeota (Brochier-Armanet et al., 2008), which are most abundant below the photic and epipelagic zone (e.g., Karner et al., 2001). Some inputs from Marine Group II (MGII), Euryarchaeota, that live in the upper 100 m of the water column, may also contribute to the sediment pool (Lincoln et al., 2014; Wang et al., 2015; Ma et al., 2020). Within this context, many regions of the ocean floor may become highly impacted by colder, deeper water column inputs. For example, a strong positive correlation was shown to exist between ocean depth and differences in TEX₈₆^H values for both surface sediments and suspended particulate organic matter in the Mediterranean Sea (Kim et al., 2015). Here TEX₈₆ dissimilarities appear to be driven by increases in the relative abundances of the GDGT-2 and isomers of crenarchaeol (see Lui et al., 2018; Sinninghe Damsté et al., 2018) coupled with decreasing abundances of GDGT-1 and GDGT-3 below the thermocline and the ammonium maxima of the water column, which produces a systematic reconstructed SST bias for deep-water surface sediments. Similar conditions have been observed for the

108 Pacific Ocean (Karner et al., 2001; Pearson et al., 2013) and Southern Atlantic (Hurley et al., 2016) where
109 peak archaeal abundances occur at 100–350 m depth. For these regions, the TEX₈₆ lipids should not produce
110 a direct response to changing SSTs. These sourcing effects have led to speculation that the TEX₈₆ ratio of
111 open ocean sediments may actually reflect deeper water column and subsurface conditions rather than SSTs
112 (Huguet et al., 2007; Lopes dos Santos et al., 2010; Kim et al., 2012a,b; Ho & Laepple, 2016; Hurley et al.,
113 2016). To address this, Schouten et al. (2013) proposed a calibration based on suspended particulate matter
114 and *in situ* water temperature from the upper 100 m of the global ocean. Both TEX₈₆^H and TEX₈₆^L (Kim et al.,
115 2012a,b) have also been re-calibrated against subsurface (0–900 m water depth) temperatures.

116
117 Other non-thermogenic driving forces impacting the production, cyclization, and relative abundance of
118 TEX₈₆-based lipids include organismal selectivity to specific growth phases and growth rates (Elling et al.,
119 2014; Hurley et al., 2016); redox conditions (Qin et al., 2015); and the incorporation of *i*GDGT from
120 archaeal communities living in the ocean floor sediments. With respect to the latter, Lipp and Hinrichs
121 (2009) demonstrated that the production of intact polar lipid GDGTs (IPL-GDGTs) by ocean floor sediment
122 microbial communities collected in the Peru Margin were distinctly different from upper water column
123 sourced CLs and that the conversion of this living pool to fossil lipids would shift TEX₈₆ ratios to higher
124 values. However, the overall impact may now be substantial as Umoh et al. (2020) found little effect to the
125 TEX₈₆ paleoclimate ratio when examining surface sediments near hydrothermal vent sites on the Southeast
126 Indian Ridge in the southern Indian Ocean. Lengger et al. (2012, 2014) also reported no significant
127 deviation between the TEX₈₆ values in sediment cores collected near the oxygen minimum zone from that
128 of the overlying water column in the Arabian Sea with near linear degradation rates of both IPLs and CLs.
129 All together, the *i*GDGT relative abundances recorded in a sediment TEX₈₆ measurement may ultimately
130 constitute a multi-variable datapoint, mixing lipid components that are themselves responses to temperature,
131 organismal substrate and metabolism dynamics, and biozone niche partitioning that spans from the ocean
132 surface to *in situ* shallow sediment community pools lastly further attenuated by depositional and diagenetic
133 processes.

134
135 While not an ideal location to create SST reconstructions, hydrothermal vents of sedimented ocean basins
136 do represent an anomalous endmember to the vast expanse of ambient ocean floor sediment where
137 paleoclimate reconstructions are commonly produced. The sedimented vent systems of Guaymas Basin,
138 Gulf of California (Figure 1) is one such site. The basin experiences high sedimentation rates ranging from
139 0.4–0.2 cm yr⁻¹ (Curry et al., 1979; Gieskes et al., 1988) due in part to the high productivity of the upper
140 water column. The ocean floor hydrothermally impacted surface sediments are also a location of active and
141 diverse microbial communities with vents that are often covered by Beggiatoa dominated microbial mats
142 (e.g. McKay et al., 2012; Meyer et al., 2013; Teske et al., 2016). These sites should in principle, enable a
143 high-resolution archaeal lipid stratigraphic record that provides optimal conditions for studying potential
144 shallow diagenetic and subseafloor interferences to common archaeal lipid-based environmental proxies.
145 The region further offers an ideal setting to compare TEX₈₆ proxy responses to *in situ* lipid production from
146 thermophilic sedimentary archaea that differ from the pelagic background communities (e.g. Schouten et
147 al., 2003). Recently, Bentley et al. (2022) produced a survey of the source and diagenetic and catagenetic
148 alteration of archaeal lipids from the Cathedral Hill hydrothermal vent complex (Figure 1) in the Guaymas
149 Basin, Gulf of California. Within the investigation, it was observed that most *i*GDGTs are sourced from the
150 overlying water column. Building on the results of Schouten et al. (2003), it was observed that these lipids
151 can become heavily turned over in the hotter portions of the vent site where they rarely survive long enough
152 to become cracked into hydrocarbon biomarkers such as biphytanes and derivatives of biphytanes. For this
153 study, we further examine the *i*GDGT lipid distributions in these near-surface ocean floor sediments to
154 determine if paleoclimate proxy signals can be impacted by the presence of subsurface archaeal
155 populations. The distribution of *i*GDGTs and their corresponding environmental proxy signals were
156 measured within the sediments along a transect at the complex. In this regard, this site offers the unique
157 opportunity to evaluate the response of TEX₈₆ and other tetraether-lipid proxies within a microbially diverse
158 sedimentary environment that is exposed to high temperature vent fluids.

159
160



162

163 **FIGURE 1** A) Location map of Guaymas Basin and the Southern Sill (red outlined box) in the Gulf of
 164 California. Cathedral Hill is marked with a yellow star. B) Photo of Cathedral Hill taken via *Alvin*. C)
 165 Schematic of the push core transect with a color-coding that is consistent for all plots throughout this paper.
 166 Maps modified from Teske et al. (2016), Dalzell et al. (2021), and Bentley et al. (2022).

167

168 2. Material and methods

169 2.1. Study location and sampling

170 Four sediment push cores were collected using HOV *Alvin* (Dive 4462; 10/22/08) at the Cathedral Hill
 171 hydrothermal vent site, located at a water depth of 1996 m in the Southern Trough of Guaymas Basin, Gulf
 172 of California (27°0.629' N, 111°24.265' W) (Figure 1). The push cores, labeled 1 to 4, were taken along a
 173 transect with ~ 2 m spacing extending outwards from microbial mat-covered sediments near the sulfide
 174 chimney complex to just outside of the microbial mat area in ambient seafloor sediment. Thermal-probe
 175 measurements were sequentially taken beside each core (Table 1). Once the push cores were brought to the
 176 surface, the sediments were subsampled into 2–3 cm-thick depth intervals, transferred to combusted glass
 177 vials, and immediately stored at -40 °C (onboard the ship) before being shipped under dry ice to the
 178 laboratory and later freeze-dried and stored at -80 °C.

179

180

181

182

183

184

185

186

187

188

189 **Table 1.** Sediment geochemical and lipid proxy data.
190

Core ^a	Depth interval (cmbsf)	Alvin dive # and core ID	Description/lithology ^b	Pore water temperature (°C) [*]	Interpolated Pore water temperature (°C) [*]	Sediment weight (g) ⁺	TLE (mg g sed ⁻¹) ⁺	Sum of IPL iGDGT (μg g ⁻¹) [†]	Sum of iGDGT (μg g ⁻¹) [‡]
1	0-2	GB4462-5	Black mud with microbial mat filaments	19	19	1.97	11.5	16.7	503.1
1	2-4	GB4462-5	Brownish-green diatomaceous mud	-	67	2.04	7.65	14.6	461.7
1	4-6	GB4462-5	Brownish-green diatomaceous mud	85	85	2.03	9.37	6.0	203.3
1	6-8	GB4462-5	Brownish-green diatomaceous mud	-	105	1.99	2.09	4.3	148.6
1	8-10	GB4462-5	Brownish-green diatomaceous mud	-	117	2.01	4.38	3.2	59.0
1	10-12	GB4462-5	Grayish-green mud	121, 124	125	2.01	1.97	1.7	48.8
1	12-15	GB4462-5	Brownish-green consolidated mud with clay shards	-	135	1.98	1.99	1.4	78.7
1	15-18	GB4462-5	Brownish-green consolidated clay	142	145	1.96	1.69	0.0	42.6
1	18-21	GB4462-5	Brownish-green consolidated clay	153	153	1.98	1.72	0.0	38.4
2	0-2	GB4462-6	Black mud with microbial mat filaments	9, 13	11	2.02	8.48	17.8	591.0
2	2-4	GB4462-6	Black mud with microbial mat filaments	-	22	1.97	8.65	7.5	266.3
2	4-6	GB4462-6	Brownish-green diatomaceous mud	20	20	1.95	2.51	2.5	87.4
2	6-8	GB4462-6	Brownish-green diatomaceous mud	-	47	1.95	3.38	3.4	69.7
2	8-10	GB4462-6	Brownish-green diatomaceous mud	-	60	1.95	1.48	2.0	48.4
2	10-12	GB4462-6	Brownish-green diatomaceous mud	69, 77	73	1.94	4.19	2.0	52.1
2	12-15	GB4462-6	Brownish-green diatomaceous mud	-	87	2.02	1.69	1.0	44.2
2	15-18	GB4462-6	Brownish-green diatomaceous mud	118	105	1.95	2.01	0.0	22.3
2	18-21	GB4462-6	Brownish-green diatomaceous mud	109	125	1.94	1.38	0.0	31.2
3	0-2	GB4462-3	Black mud with microbial mat filaments	3.2	3.2	1.96	7.31	15.3	511.3
3	2-4	GB4462-3	Brownish-green diatomaceous mud	-	8	1.96	3.91	8.3	308.9
3	4-6	GB4462-3	Brownish-green diatomaceous mud	15	15	2.00	2.86	7.0	283.5
3	6-8	GB4462-3	Brownish-green diatomaceous mud	-	26	2.02	5.00	7.5	275.3
3	8-10	GB4462-3	Brownish-green diatomaceous mud	34	34	1.97	2.02	5.7	251.1
3	10-12	GB4462-3	Brownish-green diatomaceous mud	-	43	2.01	1.86	5.8	227.7
3	12-15	GB4462-3	Brownish-green diatomaceous mud	-	54	1.94	1.78	6.5	184.6
3	15-18	GB4462-3	Brownish-green diatomaceous mud	61	66	2.01	1.43	12.3	473.1
3	18-21	GB4462-3	Brownish-green diatomaceous mud	83	80	1.96	1.98	5.2	182.3
4	0-2	GB4462-8	Black mud	0	0	1.93	3.44	16.7	485.4
4	2-4	GB4462-8	Brownish-green diatomaceous mud	1.5	8	2.01	3.17	14.6	417.8
4	4-6	GB4462-8	Brownish-green diatomaceous mud	16	16	1.95	4.00	6.0	480.6
4	6-8	GB4462-8	Brownish-green diatomaceous mud	-	18	2.02	4.19	4.3	359.7
4	8-10	GB4462-8	Brownish-green diatomaceous mud	-	21	2.02	4.76	3.2	153.5
4	10-12	GB4462-8	Brownish-green diatomaceous mud	-	23	1.95	4.84	1.7	459.5
4	12-15	GB4462-8	Brownish-green diatomaceous mud	-	25	1.95	5.74	1.4	515.2
4	15-18	GB4462-8	Sample lost during collection	-	-	-	-	0.0	503.1
4	18-21	GB4462-8	Sample lost during collection	29	-	-	-	0.0	461.7

191
192
193
194
195
196
197
198
199
200
201
202
203
204
205
206
207
208
209
210
211
212

Table 1. Sediment geochemical and lipid proxy data (continued).

Core ^a	Depth interval (cmbsf)	Alvin dive # and core ID	SUM of TEX ₈₆ cGDGT ^c (μg g ⁻¹)	TEX ₈₆ cGDGT ^c	TEX ₈₆ ^H cGDGT ^d	TEX ₈₆ ^H Reconstructed SSTs (Kim et al., 2010) ^e	RI ^f	MI ^g	TEX ₈₆ IPLGDGT ^c
1	0-2	GB4462-5	110.7	0.56	-0.25	21.2	2.44	0.34	0.58
1	2-4	GB4462-5	117.1	0.58	-0.23	22.6	2.45	0.38	0.58
1	4-6	GB4462-5	47.7	0.58	-0.24	22.3	2.48	0.36	0.55
1	6-8	GB4462-5	33.0	0.58	-0.24	22.2	2.55	0.35	0.57
1	8-10	GB4462-5	13.0	0.59	-0.23	22.9	2.60	0.34	0.72
1	10-12	GB4462-5	10.1	0.57	-0.25	21.8	2.63	0.31	0.70
1	12-15	GB4462-5	17.8	0.61	-0.22	23.8	2.65	0.37	0.69
1	15-18	GB4462-5	9.8	0.61	-0.22	23.9	2.66	0.36	-
1	18-21	GB4462-5	9.3	0.63	-0.20	24.9	2.66	0.38	-
2	0-2	GB4462-6	128.5	0.55	-0.26	20.6	2.52	0.32	0.46
2	2-4	GB4462-6	58.2	0.54	-0.27	20.4	2.52	0.32	0.58
2	4-6	GB4462-6	19.2	0.54	-0.27	20.4	2.53	0.33	0.60
2	6-8	GB4462-6	13.4	0.56	-0.25	21.5	2.68	0.29	0.71
2	8-10	GB4462-6	9.3	0.58	-0.25	21.7	2.70	0.29	0.70
2	10-12	GB4462-6	10.1	0.57	-0.24	21.9	2.71	0.28	0.68
2	12-15	GB4462-6	8.5	0.57	-0.24	21.9	2.73	0.28	0.73
2	15-18	GB4462-6	4.5	0.58	-0.23	22.6	2.68	0.31	-
2	18-21	GB4462-6	6.0	0.59	-0.23	22.8	2.74	0.28	-
3	0-2	GB4462-3	127.0	0.54	-0.27	20.2	2.41	0.37	0.53
3	2-4	GB4462-3	57.7	0.53	-0.27	19.8	2.62	0.27	0.49
3	4-6	GB4462-3	60.0	0.53	-0.27	19.9	2.53	0.31	0.56
3	6-8	GB4462-3	59.8	0.54	-0.27	20.3	2.50	0.33	0.54
3	8-10	GB4462-3	53.0	0.53	-0.27	19.9	2.54	0.31	0.61
3	10-12	GB4462-3	42.1	0.54	-0.27	20.3	2.64	0.27	0.74
3	12-15	GB4462-3	39.2	0.56	-0.25	21.5	2.56	0.30	0.69
3	15-18	GB4462-3	86.8	0.55	-0.26	20.9	2.77	0.26	0.74
3	18-21	GB4462-3	36.4	0.57	-0.25	21.6	2.68	0.29	0.66
4	0-2	GB4462-8	112.9	0.54	-0.27	20.4	2.43	0.35	0.54
4	2-4	GB4462-8	85.3	0.53	-0.27	20.0	2.59	0.30	0.37
4	4-6	GB4462-8	102.7	0.54	-0.27	20.2	2.55	0.31	0.43
4	6-8	GB4462-8	70.8	0.52	-0.28	19.3	2.55	0.29	0.45
4	8-10	GB4462-8	26.6	0.53	-0.27	19.9	2.69	0.26	-
4	10-12	GB4462-8	91.0	0.53	-0.27	19.8	2.54	0.30	-
4	12-15	GB4462-8	73.7	0.53	-0.28	19.7	2.90	0.20	-
4	15-18	GB4462-8	110.7	-	-	-	-	-	-
4	18-21	GB4462-8	117.1	-	-	-	-	-	-

^a Also reported in Bentley et al. (2022).

[†] Sum of GDGT-1, -2, -3, -4, -5, and -5' (Table S1).

[‡] Sum of all detected 1G- and 2G-GDGTs (Table S3).

^a Collected core numbers are relabelled in the sample name to reflect a relative transect position (1-4).

^b Sediment lithology based on freeze-dried sediments.

^c TEX₈₆ = (GDGT-2 + GDGT-3 + GDGT-5')/(GDGT-1 + GDGT-2 + GDGT-3 + GDGT-5'), (Schouten et al., 2002) applied to both core GDGTs and 1-glycosyl-GDGTs (also referred to as *M*TEX₈₆ in section 3.4).

^d TEX₈₆^H = log ((GDGT-2 + GDGT-3 + GDGT-5')/(GDGT-1 + GDGT-2 + GDGT-3 + GDGT-5')), for sediments outside low latitudes (Kim et al., 2010).

^e Following the mean annual sea surface calibration of 0 m water depth (SST = 68.4 × TEX₈₆^H + 38.6) of Kim et al. (2010).

^f Ring index (RI) = 0×(GDGT-0) + 1×(GDGT-1) + 2×(GDGT-2) + 3×(GDGT-3) + 4×(GDGT-4) + 5×(GDGT-5)/ ΣGDGTs, adapted from Pearson et al. (2004) and promoted by Zeng et al. (2016).

^g Methane index (MI) = (GDGT-1 + GDGT-2 + GDGT-3)/(GDGT-1 + GDGT-2 + GDGT-3 + GDGT-5 + GDGT-5') by Zhang et al. (2011).

2.2. Lipid extraction

Lipid extractions followed a modified Bligh and Dyer protocol laid out in Bentley et al. (2022) and following Sturt et al. (2004). A subsample of freeze-dried sediment was added to a Teflon® centrifuge tube followed by the addition of 6 ml of mix A solvent solution comprising of 2:1:0.8 v/v/v methanol (MeOH), dichloromethane (DCM), and phosphate buffer (5.5 g L⁻¹ Na₂HPO₄; Avantor Performance Materials, LLC. adjusted to pH of 7.4 with HCl; Anachemia Co.). The solvent sediment mixture was further spiked with 1-alkyl-2-acetoxy-*sn*-glycero-3-phosphocholine (PAF) recovery standard purchased from Avanti Polar Lipids, Inc. The slurry was sonicated for 5 min then centrifuged for 5 min at 1250 rpm. The resulting supernatant was added to a separatory funnel. This procedure was performed twice before being joined by two replicate extractions using mix B, a 2:1:0.8; v/v/v solution of MeOH, DCM, and trichloroacetic acid buffer (50 g L⁻¹ C₂HCl₃O₂; Avantor Performance Materials, LLC. of pH 2) and a final two replicate extractions using mix C, a 5:1 v/v solution of MeOH and DCM. Once complete, the combined A, B, and C. For each step, the organic fraction was collected in a beaker, and the combination of mix A, B, and C were subjected to 10 ml of DCM and H₂O (MilliQ) to achieve separation. The organic phase was drawn off and the water was extracted using 3 DCM washes, drawing off the organic phase after each wash. The organic phase was then back-extracted with H₂O to ensure purity. The resulting organic phase was then evaporated to dryness at 60 °C under dry nitrogen. The resulting total lipid extract (TLE) was transferred to pre-weighed autosampler vials using DCM:MeOH 1:1 v/v, spiked with 1, 2-diheneicosanoyl-*sn*-glycero-3-phosphocholine (C₂₁-PC; Avanti Polar Lipids, Inc.) and stored at -20 °C.

2.3. High performance liquid chromatography – mass spectrometry (HPLC-MS)

Mass spectrometric analyses were performed on an Agilent Technologies 1260 Infinity II HPLC coupled to an Agilent Technologies 6530 quadrupole time-of-flight mass spectrometer (qToF-MS) operated in positive mode. Chromatographic separation used a reverse-phase method outlined by Zhu et al. (2013). The HPLC was fitted with an Agilent Technologies ZORBAX RRHD Eclipse Plus C₁₈ (2.1 mm × 150 mm × 1.8 μm) reverse phase column and guard column maintained at 45 °C. The sample injection solvent was methanol. An aliquot of each sample representing 1% of the TLE was analyzed. A 0.25 mL min⁻¹ flow rate was established with mobile phase A consisting of methanol/formic acid/ammonium hydroxide (100:0.04:0.10 v/v/v) held at 100% for 10 min, thereafter mixed following a linear gradient with mobile phase B (propan-2-ol/formic acid/ammonium hydroxide (100:0.04:0.10 v/v/v) to 24%, 65%, and 70% over 5-, 75-, and 15-min intervals, respectively. Each sample run was finished by re-equilibrating the system with 100% mobile phase A for 15 min. The effluent was ionized by an electrospray ionization source with a gas temperature of 300 °C, a 3 L min⁻¹ drying gas flow, and a 5.33 μA source current. The mass spectrometer was set to a 100–3000 *m/z* scan range in positive mode in an untargeted method with 10 ppb resolution to simultaneously resolve both archaeal IPLs and CLs.

Analyte identification was achieved by accurate mass resolution, mass spectral analysis using Agilent Technology's MassHunter software, and comparison of fragmentation patterns with the literature (e.g., Knappy et al., 2009; Liu et al., 2010; Yoshinaga et al., 2011 – see Bentley et al., 2022 for further details). Mass fragments consistent with the loss of a biphytane (*m/z* 743.7) were screened for all archaeal lipids. Quantification was achieved by summing the integration peak areas of [M+H]⁺, [M+NH₄]⁺, and [M+Na]⁺ adducts for the respective IPLs and CLs of interest. Concentration values were obtained relative to the internal C₂₁-PC standard and reported in μg/g dry sediment weight. Response factors were determined by a series of injections of a standard solution containing: PAF, C₂₁-PC, 1,2-diacyl-3-O-(α-D-galactosyl-1-6)-β-D-galactosyl-*sn*-glycerol (DGDG), 1,2-diacyl-3-O-β-D-galactosyl-*sn*-glycerol (MGDG), 1,2-di-O-phytan-3-yl-*sn*-glycerol (Archaeol), 1',3'-bis[1,2-dimyristoyl-*sn*-glycero-3-phospho]-glycerol (14:0 Cardiolipin) from Avanti Polar Lipids, Inc., USA, and 2,2'-di-O-decyl-3,3'-di-O-(1'',ω''-eicosanyl)-1,1'-di-(rac-glycerol) (C₄₆-GTGT) from Pandion Laboratories, LLC in amounts ranging from 100 pg to 30 ng. Response factors were calculated relative to the C₂₁-PC, and the appropriate correction factor was then applied to the lipid class of interest.

A series of samples were re-run to identify or confirm deviations in the data set. The variations between the concentrations of GDGTs in the re-run and the initial runs yielded a maximum difference of ~ ± 4 μg g⁻¹ per

GDGT compound, providing confidence in the initial results and confirming the presence of two outliers in the data set (Bentley et al., 2022). These outliers are Core 4 at 8-10 cm, with abnormally low concentrations of all compounds that are likely ion suppression from a sample heavily impregnated with oil, and Core 3 at 15–18 cm, which contains relatively high lipid concentrations that are yet to be explained.

3. Results and Discussion

3.1. Archaeal lipid diversity and turnover

The Cathedral Hill transect sediments have *i*GDGTs containing 0–4 cyclopentyl (GDGT 0–4) as well as crenarchaeol (Cren) and the isomer of crenarchaeol (Cren') that contains five rings (four cyclopentyl and one cyclohexyl moiety) (Table S1). Branched GDGTs (*br*GDGTs) including Ia-c, IIa-c, and IIIa were found to have discontinuous and/or low absolute abundances, with some compound classes not being detected (i.e. *br*GDGT-IIIb; Table S2). The *br*GDGTs are therefore not further examined in this study. For cores 1 to 3 the concentrations of nearly all *i*GDGT compounds systematically decrease with depth (Figure 2). Bentley et al. (2022) established the sedimentation of archaeal lipids from the upper water column as being uniform both in terms of spatial loading across the length of the transect as well as over an inferred 52.5–105 yrs of sedimentation as penetrated by the length of the push core (based on sedimentation rates). From this, it is estimated that $\sim 70.57 \pm 23.5 \mu\text{g } i\text{GDGTs g}^{-1} \text{ sed yr}^{-1}$ is being deposited on the seafloor from the overlying water column. However, for cores closest to the vent site, lipid abundances exhibited a much sharper decrease with depth, which Bentley et al. (2022) attribute to the turnover of archaeal lipids coupled to, but not directly caused by, hydrothermalism. For cores 1 and 2, losses reach as high as 94% within the upper 21 cmbsf (cm below seafloor). The lipid loss is less severe for core 3 at $\sim 60\%$. For the ambient core 4, *i*GDGTs have similar down core stratigraphic trends with a near-consistent average of $400 \mu\text{g g}^{-1}$ sediment concentration and no systematic loss of lipids.

Due to the high temperature conditions of the vent fluids at Cathedral Hill, the identified archaeal *i*GDGT-based IPLs within the sediments most likely represent the composition of cellular membrane material from archaeal communities living in the sediments. These lipids have exclusively monoglycosyl (1G) or diglycosyl (2G) head groups linked to a 2,3-sn-glycerol. Within the pyrolytic environment, the transformation of IPL *i*GDGTs could hypothetically add to the core *i*GDGT lipid pool. Similar to CLs, the 1G-GDGTs contain 0-4 cyclopentyl moieties and include Cren and Cren'. Surface concentrations of these lipids are $\sim 15 \mu\text{g g}^{-1} \text{ sed.}$ in cores 1 to 3 (residing within the microbial mat) and $11 \mu\text{g g}^{-1} \text{ sed.}$ for core 4 (Table S2). Also similar to the CLs, the archaeal IPL concentrations decrease down core and are closely coupled to increasing porewater temperatures (Table S2). For cores 1 and 2, the maximum depths for detectable 1G-GDGTs are 15–18 and 12–15 cmbsf, corresponding to vent porewater temperatures of 145 and 87 °C, respectively. In core 3, 1G-GDGTs persist down core with a consistent lipid depletion that reaches its lowest concentration of $5.22 \mu\text{g g}^{-1} \text{ sed.}$ in the bottom of the core at 18–21 cmbsf sediment depth where porewater temperatures rise to 80 °C. In core 4, which is most similar to the ambient ocean bottom conditions and falls outside of the area covered by the microbial mat, the lipid concentrations average is $\sim 8 \mu\text{g g}^{-1} \text{ sed.}$ across the depth of the core. The 2G-GDGTs have 0 to 2 cyclopentyl rings that for cores 1 and 2 are restricted to the upper 4 to 6 cmbsf. These lipids are not further investigated in this study as 2G-GDGTs are of limited abundance (max summed concentrations $< 2 \mu\text{g g}^{-1} \text{ sed.}$) and their structural diversities negligibly affect isoprenoid-based proxies.

Lipid-based proxies for the calibration or reconstruction of paleoclimate records such as TEX₈₆, BIT, CBT, and MBT, are based on environmentally scaled contributions of select GDGT compounds. These proxies could be negatively impacted should other ocean floor sediment systems experience high rates of lipid turnover (Lengger et al., 2014). To evaluate whether down-core depletions of lipid concentrations impacted tetraether-based proxies, the concentrations of the highly abundant GDGT-0 was plotted relative to the TEX₈₆ ratio lipids (*i*GDGT-1, -2, -3, and Cren') (Figure 3A). For figure 3A, straight lines in the logarithmic plot indicate near-equal depletion rates between the paired x- and y-axis lipid classes. Similarly, parallel slopes for the various lipid pairs also indicates near-equal depletion rates, with vertical offsets between pairs marking different initial starting abundances of the compared lipid. In this regard, *i*GDGT-0, -1, -2, and Cren' have undergone the same rate of turnover. However, the depletion rate of *i*GDGT-3's is lower than

that of other lipid classes for cores 1 and 2. Although, this may represent a distinct resilience to turnover, we suggest it instead results from overprinting by the subsurface hyperthermophilic archaeal community (see below).

To better track changes across each core, the degradation rate constants (k') of TEX₈₆ lipid classes were calculated for each push core (Figure S2; Table S3) using a first-order kinetic model:

$$C_t = C_i e^{-k't} \quad (1)$$

in which C_t and C_i are concentration at time (t) and the initial concentration, respectively (e.g. Schouten et al., 2010). Rearranging Eq. 1, the k' were calculated as

$$k' = (-\ln[C_t/C_i])/t \quad (2)$$

From these data, it is evident that the down core concentrations of each lipid decrease at equivalent rates (i.e. they have the same slopes for their rates of decay $s^2 = 0.2$). the exception to this is core 2, which independent of two outliers has different decay paths for GDGT-3 and GDGT-5. This is consistent with the TEX₈₆ *i*GDGT lipid classes largely being removed from the sediment lipid pool in a non-selective manner.

Based on these results, the TEX₈₆, ring index (RI), and methane index (MI) values were plotted against their respective summed *i*GDGTs lipid concentrations (Fig 3B–D). For samples located within the habitable zone (having porewaters ranging from 0–123 °C; Kashefi and Lovley, 2003), no correlation is observed between the lipid abundances and proxy ratios of TEX₈₆, RI, or MI (Figure 3B–D). This further suggests these proxies are not affected by turnover in the habitable zone. However, once sediment burial reaches beyond the habitable zone, TEX₈₆ ratios trend to higher values (similarly also reflected in GDGT-3 concentration trends of Figure 3A). Collectively, these data strongly indicate that archaeal lipid turnover is largely nonselective of the TEX₈₆ lipid classes and will therefore theoretically not in and of themselves significantly impact archaeal lipid paleoclimate proxy reconstructions.

Apart from paleoclimate reconstructions, archaeal lipid CLs are sometimes used to resolve aspects of localized biogeochemical cycles within sediments. To this end, the location and degree of anaerobic oxidation of methane (AOM) is determined by methane and archaeal lipid carbon isotope measures (e.g. Boetius et al., 2000; Schouten et al., 2003; Stadnitskaia et al., 2008; Biddle et al., 2012) as well as by the proportional abundances of core GDGTs (*c*GDGTs) in the form of the MI (Zhang et al., 2011; Carr et al., 2018; Petrick et al., 2019). With respect to the latter, the MI proxy is used to differentiate regions of normal marine (with values between 0–0.3) and active AOM conditions in and around cold seeps (where values >0.5–1 are reported for gas hydrate impacted sediments and subsurface environments with high AOM levels). To our knowledge, the use of this proxy for hydrothermal vent systems has not been thoroughly investigated even though this microbial process has been well documented at Guaymas Basin. For example, highly ¹³C-depleted CLs reaching up to -70‰ in hydrothermal vent sediments with porewater temperatures as high as 95 °C indicates thermophilic archaea actively engaging in AOM (Schouten et al., 2003). Biddle et al. (2012) through the detection of relevant archaeal communities by 16S RNA in conjunction with highly depleted methane carbon isotope values determined active AOM spanning 35 to 90 °C porewater conditions. AOM is not likely to be the dominant form of carbon and sulfur metabolism as it generally accounts for less than 5% of sulfate reduction (Kallmeyer and Boetius, 2004). When applying the MI to the Cathedral Hill push core transect survey low values (ranging from 0.2–0.38; Table 1) are recorded with no correspondence to thermal controls across the vent transect (Figure 4). Although, it could be considered that the low values arise from a lack of AOM within these sediments the low MI values are consistent with a high upper water column *i*GDGTs loading as estimated by Bentley et al. (2022).

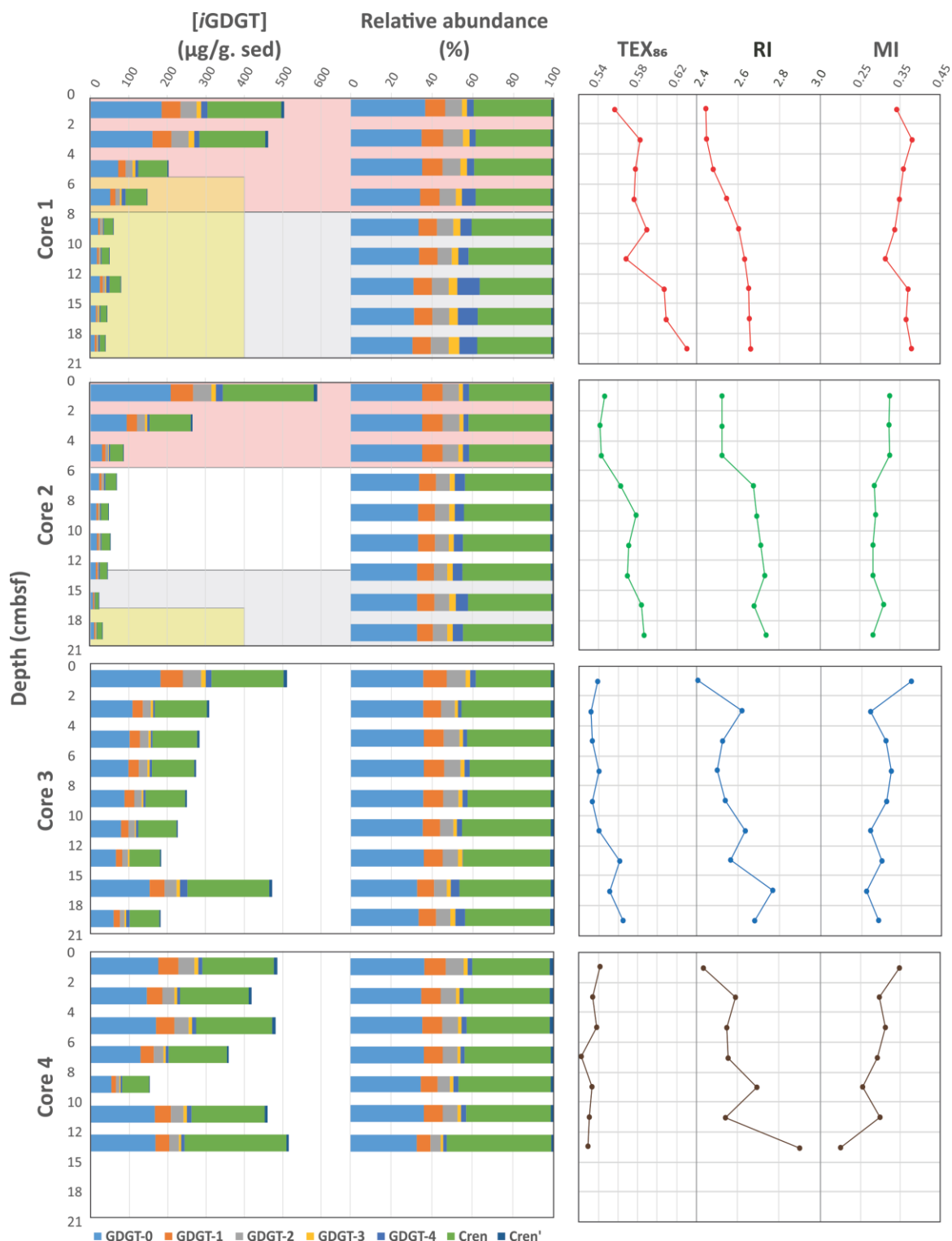
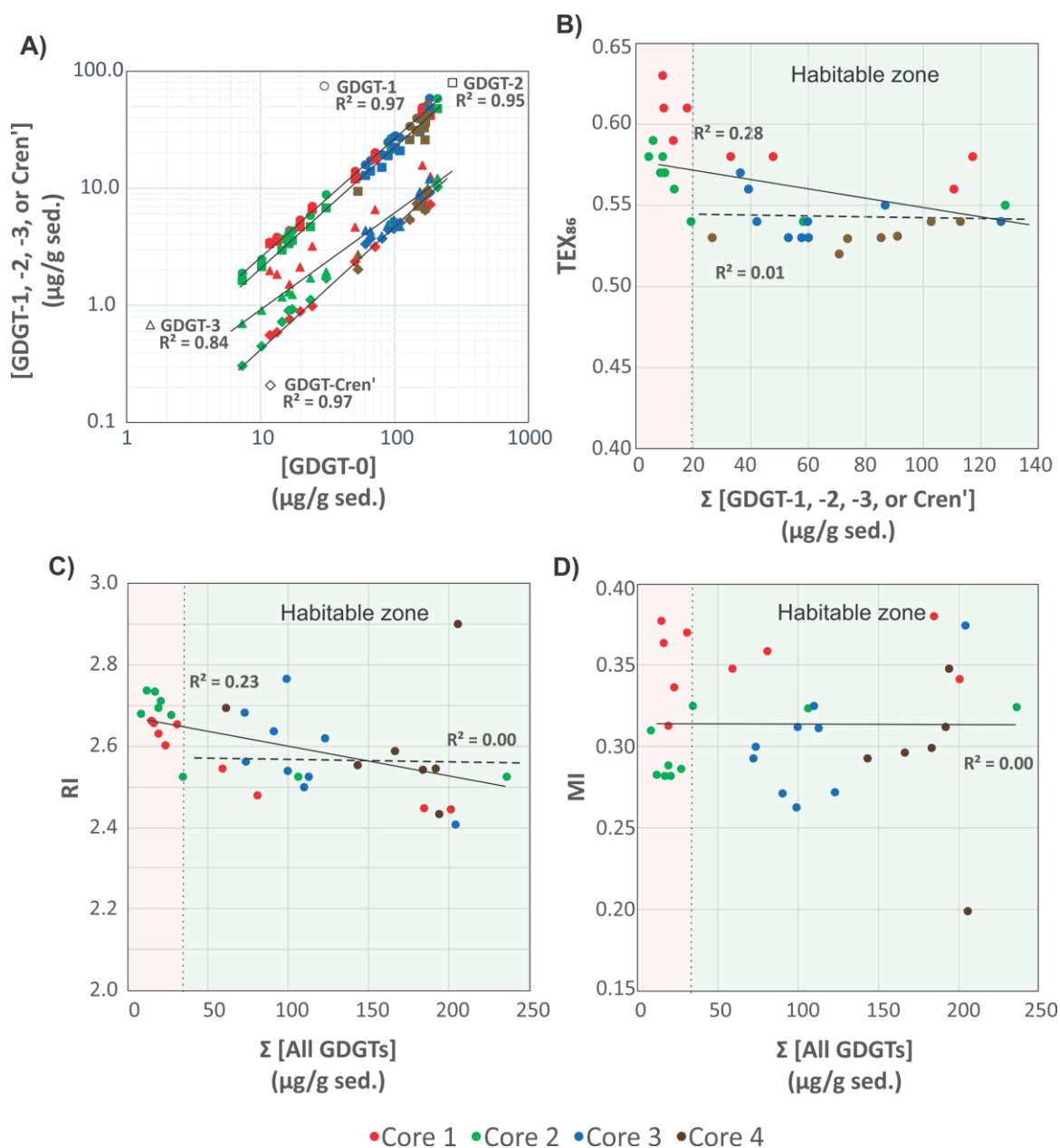


FIGURE 2. Down core profiles of the Cathedral Hill core *i*GDGTs absolute and relative lipid abundances and their generated *i*GDGT proxies: TEX₈₆, RI, and MI. Pink regions indicate transect intervals within zones of active GDGT lipid heterotrophy (Bentley et al., 2022). Grey regions mark regions where porewater temperatures exceed 123 °C marking a zone beyond the known upper thermal limit of life (Kashefi and Lovley, 2003). Yellow fields indicate regions where oil generation and hydrocarbon degradation have been noted to occur (Dalzell et al., 2021).

400
401



402
403

404 **FIGURE 3.** A) Comparison of TEX_{86} lipid concentrations GDGT-1 (circles), -2 (squares), -3 (triangles),
405 and Cren' (diamonds) relative to the GDGT-0. Comparison of B) TEX_{86} , C) RI, and D) MI proxy values
406 relative to summed *i*GDGTs abundances of the Cathedral Hill transect cores. Light green and pink regions
407 indicate areas within and outside the habitable zone of life. Solid and dotted regression lines mark the total
408 number of samples investigated for this study ($n=34$) and those that only reside within the habitable zone
409 where up to 94% of the archaeal lipid turnover occurs ($n=22$), respectively.

410
411
412

3.2. TEX₈₆ and reconstructed SSTs

McClymont et al. (2012) reported a GDGT-based reconstructed annual SSTs of 16–18 °C from particulate organic matter collected in ambient sediment traps in the Guaymas Basin during an annual cycle from 1996–1997. The reconstructed temperatures followed the calibration model for sediments outside of polar regions proposed by Kim et al. (2010). These authors demonstrated the temperatures derived from the TEX₈₆ reconstruction were significantly lower than those produced by the closely co-varying U₃₇^{kl} paleoclimate proxy, and satellite measured estimates that jointly estimated a mean annual sea surface temperature (MASST) of 23 °C. The longer 21-year (1982–2004) satellite-derived MASST is also reported to be higher at 24 °C (Herrera-Cervantes et al., 2007). Although, the sites and time frames of these surveys do not match that of the Cathedral Hill survey, they do provide context to what our reconstructed TEX₈₆ values should record.

The high sedimentation rate at Cathedral Hill has resulted in near homogenous inputs of organic matter from the upper water column across the transect area (Dalzell et al., 2021; Bentley et al., 2022). Therefore, TEX₈₆ reconstructions should produce equivalent cross-transect trends with sediment depth. Nonetheless, as with changes in the archaeal lipid concentrations, the profiles of *i*GDGT proxies TEX₈₆ and RI of the transect similarly have down core trends (Figure 2; Bentley et al., 2022). For core 4, TEX₈₆ span a narrow range of values (n=7; 0.52–0.54, avg. 0.53 ± 0.01 ; Figure 4A) across a period of ~ 37.5 to 75 yrs. corresponding to the depth of the cores. To a slightly lesser degree, the core top (0–2 cmbsf) across the transect also display near-equal values to core 4 (n=4; 0.56–0.54; avg. 0.55 ± 0.01). These values mark a TEX₈₆^H reconstructed mean annual SST of 19.3–20.4 °C following the Kim et al. (2010) calibration model (Table 1). However, the TEX₈₆ values recorded in cores 1 to 3 at Cathedral Hill have considerably larger ranges with values spanning from 0.53 to 0.63 (Table 1) that systematically increase with rising porewater temperatures ($R^2 = 0.83$; Table 1; Figure 2 and 4A). This increase is most noticeable in core 1 where the highest TEX₈₆ values are obtained from the bottom core sediments (10–21 cmbsf; marking the non-habitable zone) where TEX₈₆ values span 0.57–0.63 (Table 1; Fig 4A) corresponding to a TEX₈₆^H reconstructed SST change of 3.1 °C marking a range from 21.8 to 24.9 °C (Table 1). The fundamental driver for the proxy's is likely influenced by the archaeal community composition that is responding to their exposure to *in situ* vent fluid temperatures (Figure 4).

Two mechanisms are considered for the observed proxy variations. The first is that progressive ring-loss due to carbon-carbon bond cleavage of pentacyclic rings moieties by exposure to the sharp geothermal gradient acts to systematically attenuate the *i*GDGT lipid pool. Hydrous pyrolysis experiments conducted by Schouten et al. (2004) demonstrated that at extreme temperatures (ca. >160 °C), TEX₈₆ values become negatively impacted by the preferential destruction of polycyclic GDGTs. Such losses produce progressively lower ratio values. Although, the transect sediment porewaters do not reach the pyrolytic temperatures of the Schouten et al. (2004) experiment, they are high enough to generate hydrocarbons (Dalzell et al., 2021) and thermochemically degrade *i*GDGTs in the hottest regions of the transect they are also more long-lived than what is produced from a laboratory experiment. However, the observed stratigraphic TEX₈₆ trends do not match those of predicted ring loss as the values increase rather than decrease in relation to elevated porewater condition. Nonetheless, the thermochemical oxidative loss of GDGTs and its effect on the TEX₈₆ ratio is further explored below (section 3.4).

The second mechanism is that subsurface microbial communities donate enough core GDGTs to overprint the detrital signal source. The RI (Figure 4B) values were similarly compared to recorded porewater temperatures to better interpret the TEX₈₆ trends and to ensure that the Cathedral Hill reconstructed temperatures are influenced by the subsurface microbial community. In this regard, RI is used to monitor the adaptive response of an archaeal community at the hydrothermal vent site. Lipid cyclization is an adaptive response to changing environmental temperature or acidity in which an archaeon increases its rigidity by decreasing the fluidity and permeability of its cellular membrane that, therefore, also further regulates the flow of solutes and nutrients in and out of the cell (Gliozzi et al., 1983; De Rosa and Gambacorta, 1988; Uda et al., 2001; Schouten et al., 2002; Macalady et al., 2004; Boyd et al., 2013). Both cores 1 and 2 have RI values highly correlated to temperature ($R^2 = 0.87$ and 0.75 , respectively) consistent with heat stress adaption. This same was also observed in the Guaymas Basin by Schouten et al. (2003) who reported an increase in the RI of core lipid GDGTs with *in situ* temperature. As such, a significant

469 proportion of the measured *i*GDGTs likely emanates from archaeal communities living in the shallow
 470 sediments of Cathedral Hill. As such, the lipid cyclization pattern may reflect stratigraphically discrete
 471 thermophilic to hyperthermophilic communities that are selectively adapted to more extreme temperature
 472 conditions (see Bentley et al., 2022 for further discussion on the lipid-based taxonomic make-up of the vent
 473 site).
 474
 475

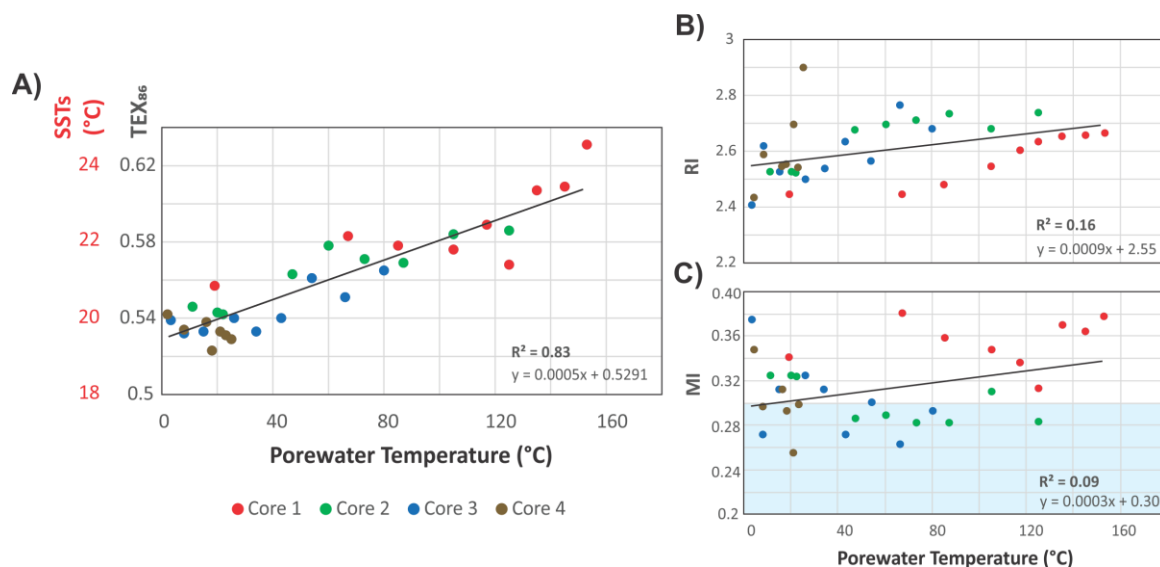


FIGURE 4. Cross plots of A) TEX_{86} , B) RI, and C) MI, *i*GDGT proxies versus porewater temperature. TEX_{86}^H reconstructed MASSTs are based on Kim et al. (2010). Blue field indicates MI values for normal marine conditions (Zang et al., 2011).

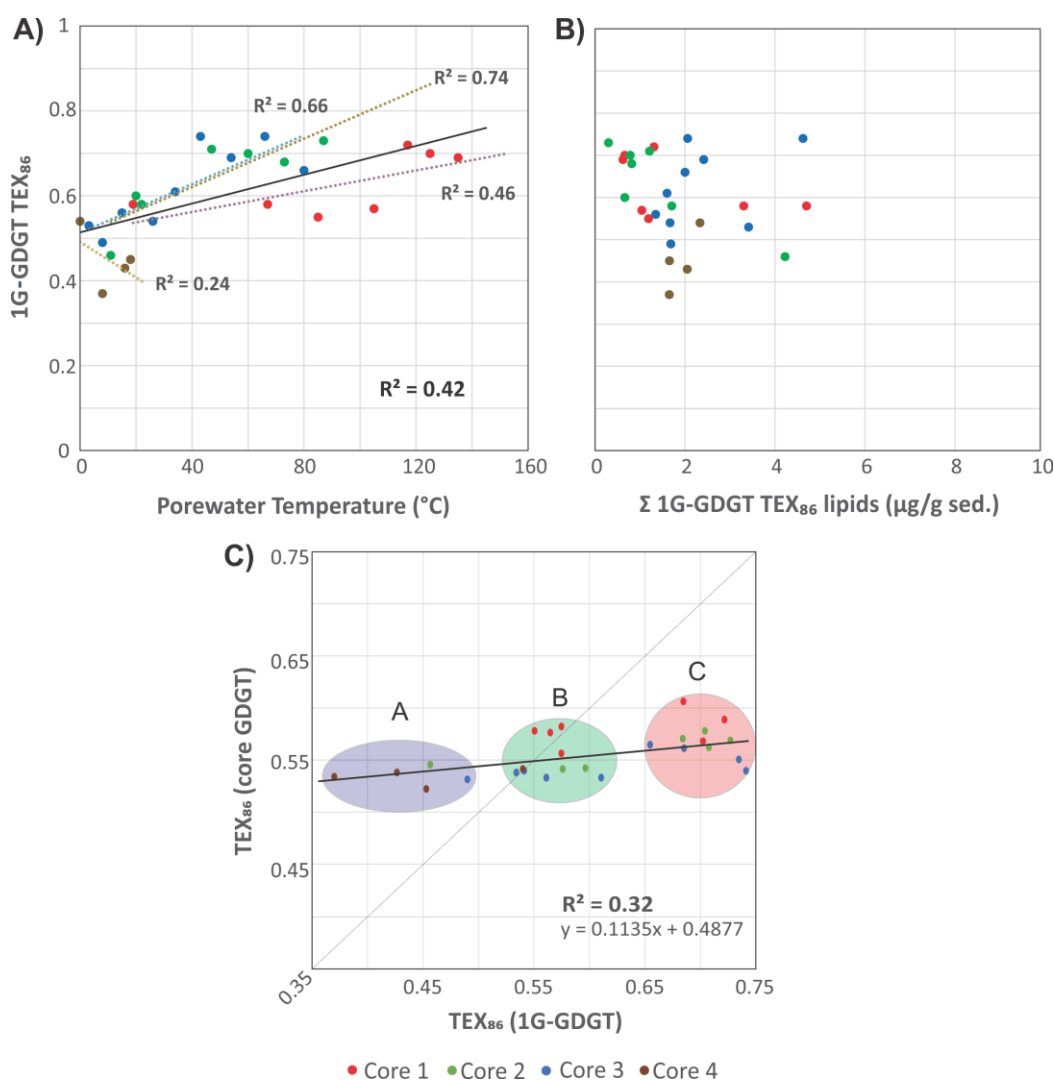
476 3.3. Lipid signal sourcing

477 To evaluate the sources of measured archaeal lipids, CL and IPLTEX_{86} (the ratio applied to IPLs that contain
 478 equivalent core lipids) indices were compared as signal responses from their respective pools of living and
 479 dead cellular debris (Figure 5). For cores 1, 2, and 3 the 1G-*i*GDGT IPLTEX_{86} measures are positively
 480 correlated with temperature ($R^2 = 0.46, 0.74,$ and 0.66 , respectively; Figure 5A). In this regard, 1G-*i*GDGT
 481 IPLTEX_{86} ratio appears to be largely influenced by *in situ* porewater temperatures as well as may by the
 482 archaeal community ecology of the vent system. Factors such as community composition and adaptation
 483 may further impact the IPLTEX_{86} ratio as the rates of changes between cores 1–3 are not the same. Similar to
 484 the CLTEX_{86} values, the IPLTEX_{86} is not correlated to their summed TEX_{86} lipid abundances (Figure 5B).
 485 Such a condition is largely consistent with the living lipid pool being modified by the archaeal community's
 486 response to thermal stress and not by subsequent thermal-oxidative transformation occurring shortly after
 487 cell death.

488
 489 The IPL and CL lipids of transect samples can be further grouped into three clusters (A, B, C), suggesting a
 490 mixed signal for the sourcing of archaeal GDGTs from both the living and dead pools of archaea (Figure
 491 5C). In this plot, we assume that clusters falling on the 1:1 line indicate the living biota can equally
 492 contribute to the dead pool of total recovered GDGTs. Those off-axis contribute either less or more to one
 493 or the other lipid pool. The three clusters mark unique thermal zones within the transect area with cluster A
 494 being composed of the ambient core 2 to 4 seafloor surface samples; cluster B marking a mix of
 495 intermediate temperature samples from all cores; and cluster C being composed of high temperatures
 496 samples. The lipid groups likely mark distinct archaeal communities. As cluster B resides on the 1:1 line,
 497 the TEX_{86} core lipids likely have a mix of detrital and *in situ* inputs. Cluster C, however, appears likely

dominated by *in situ* lipid production. The hyperthermophilic *Methanopyrus kandleri*, recovered from other Guaymas Basin sites (Teske et al., 2014), may represent one such archaeon contributing to the cluster C lipid pool. The thermal zonation and equivalent directionality of the resulting ratios (i.e., both CL and IPL TEX₈₆ ratios increase with porewater temperature) further supports overprinting of the original CL TEX₈₆ sea surface signal by the ocean bottom sediment archaeal community as a mechanism for the observed CL TEX₈₆ trends.

Collectively, these results suggest the source of the archaeal CLs measured in the TEX₈₆ and RI indices progressively become more dominated by subsurface microbial communities adapted to the hotter hydrothermal vent fluids. Our results also indicate that in select natural environments, such as hydrothermal vent complexes, the TEX₈₆ SST-proxy may entirely record ocean bottom sediment porewater temperatures. To our knowledge, a clear case of overprinting to this level has not yet been demonstrated.



511

FIGURE 5. Cross plots of 1G-iGDGTs IPL TEX₈₆ versus (A) porewater temperatures and (B) the concentration of 1G-iGDGTs in the sediments. C) TEX₈₆ proxy of core GDGTs vs 1G-GDGTs. Clusters A–C may represent different archaeal communities that are providing varying inputs of iGDGT to the core GDGT lipid pool. The dotted trendline is the partial least square regression of the complete core lipid TEX₈₆ data set. The solid line marks the 1:1 CL to IPL proxy correspondence indicating both allochthonous and autochthonous sources contribute equally to the core GDGT lipid pool.

3.4. TEX₈₆ overprint corrections

The measured TEX₈₆ ($M\text{TEX}_{86}$) value of the Cathedral Hill sediments is herein considered to be a weighted sum of a sea surface TEX₈₆ ($SS\text{TEX}_{86}$) value acquired from lipids sourced in the upper water column that is further modified by a component of the deeper water column sourced core lipids ($WC\text{TEX}_{86}$) as well as by additions of archaeal lipids from the benthic and subsurface microbial communities ($Sed\text{TEX}_{86}$). These ratio loadings are collectively also potentially further modified by diagenetic influences in the ocean bottom sediments. Over the cumulative sediment burial period and in consideration of the measured porewater temperatures of the Cathedral Hill push core sediments, these influences include the selective loss of lipids by their binding into protokerogen (K) and by potential changes due to the loss of lipid by turnover (ϕ ; section 3.1). Additional catagenetic effects from thermochemical alteration of lipids (θ) may also attenuate the sum of sedimentary core lipids by their exposure to high temperature vent fluids. Collectively, these effects are considered to form the following relationship:

$$M\text{TEX}_{86} = \frac{a_{SS}\text{TEX}_{86} + b_{WC}\text{TEX}_{86} + c(d_{0-n})_{Sed}\text{TEX}_{86}}{\phi + K + \theta} \quad (3)$$

where a , b , and c , are measured scaling parameters for lipid loading and ϕ , K , and θ are diagenetic and catagenetic alteration parameters. Solving for $SS\text{TEX}_{86}$:

$$SS\text{TEX}_{86} = \frac{M\text{TEX}_{86}(\phi + K + \theta)}{a} - \frac{b_{WC}\text{TEX}_{86} + c(d_{0-n})_{Sed}\text{TEX}_{86}}{a} \quad (4)$$

In this regard, a portion of the archaeal community from the upper water column, presumably initially sourced of IPLs, and an additional community inhabiting the ocean floor sediments were assumed to eventually die with their respective IPLs gradually hydrolyze, joining the CL pool where they further contribute to the observed $M\text{TEX}_{86}$ value. For this study, no data was collected to calculate $b_{WC}\text{TEX}_{86}$ and its potential impact on $M\text{TEX}_{86}$ cannot be further considered in this study. However, it is highly likely, given the longer residence times for glycosidic-based headgroups of the identified archaeal IPLs and their relatively short settling time through the water column (Lengger et al., 2012; Xie et al., 2013) that a component of this lipid source was already mixed with the $Sed\text{TEX}_{86}$ contribution. For this study, $Sed\text{TEX}_{86}$ is an $IPL\text{TEX}_{86}$ ratio based on detected 1G-GDGT-1, -2, -3, Cren' and 2G-GDGT-1, -2, as present in the original paleoclimate proxy (Table 1; Figure 6). Testing the removal of 2G-GDGTs lipids, which have a low absolute concentration ($<2 \mu\text{g g}^{-1} \text{ sed.}$) and shallow stratigraphic zones of occurrence (section 3.1; Table S2), yielded a negligible $<1^\circ\text{C}$ change in the summed average reconstructed SST.

The $c(d_{0-n})$ measured scaling parameter was calculated as

$$c(d_{0-n}) = \sum_{i=0}^n \left(\frac{[\text{GDGTs}_{IPL-\text{TEX}_{86} \text{ lipids}}]_n}{[\text{GDGTs}_{CL-\text{TEX}_{86} \text{ lipids}}]_{0-2cm}} \right) \quad (5)$$

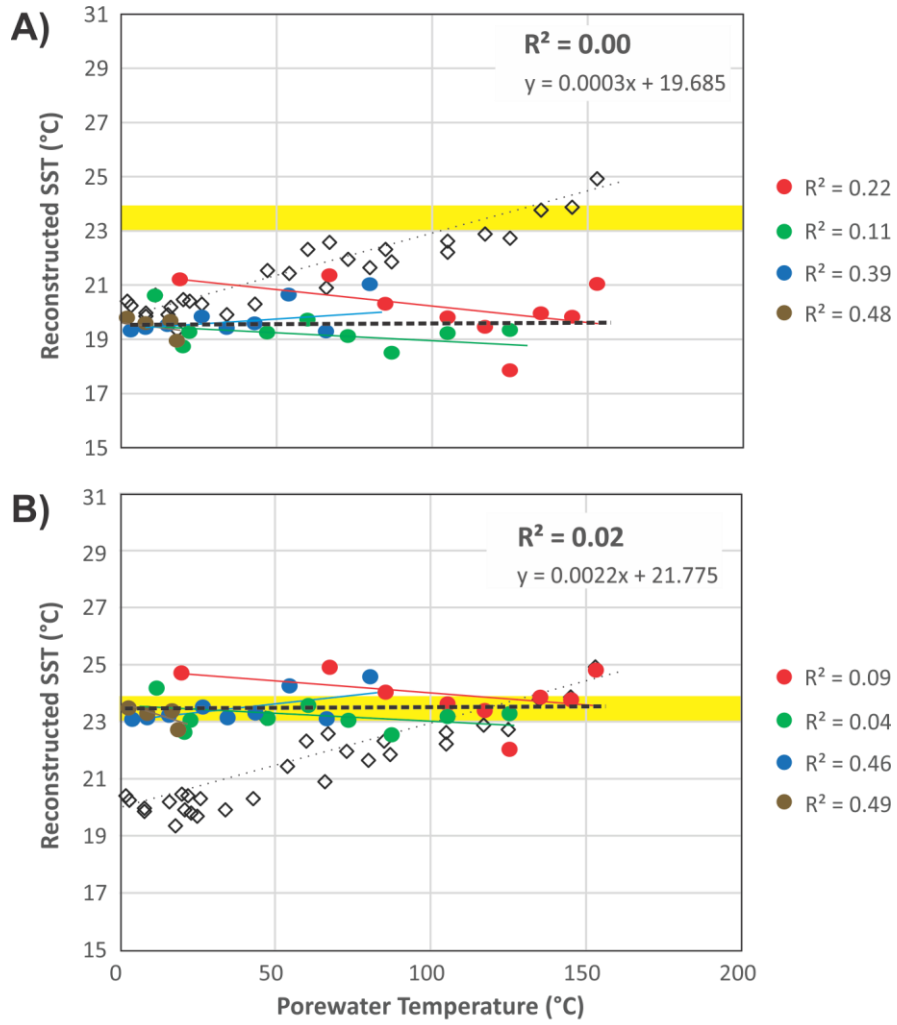
using the summed concentrations of 1G- and 2G-GDGTs that have the potential to become converted to $c\text{GDGTs}$ by progressive burial diagenesis and d_{0-n} marking the range of sampled sediment depths, with 0 being the 0-2cmbsf core top and n the deepest point of sediment burial. These intervals are divided by the water column input of TEX₈₆ lipids ($[\text{GDGTs}_{CL-\text{TEX}_{86} \text{ lipids}}]_{0-2cm}$) estimated to be $120 \mu\text{g g}^{-1} \text{ sed.}$ based on their average measured concentration across the four-core transect. The function assumes the surface sediment does not hydrolyze its IPL-GDGTs to CLs (Table 2). When applied to Eq. 4 and further excluding ϕ , K , and θ , the $SS+WC\text{TEX}_{86}^H$ reconstructed SSTs average $19.68 \pm 0.79^\circ\text{C}$ (Table 2; Figure 6A) with the total samples having an unchanging depth profile that mirrors the range of values measured in the ambient sediments of core 4 (Figure 2).

The selective lipid removal by diagenetic and catagenetic processes theoretically may also affect the TEX₈₆ value; however, their perspective impact on the directionality and magnitude of the ratio are difficult to predict and equally hard to discretely measure. Although the loss of GDGTs to protokerogen formation

could potentially impact the ratio, it was shown to be a negligible sink for the lipids (Bentley et al., 2022). As such, the K parameter in Eqs. 3 and 4 was therefore assigned a 0 value. Due to the high geothermal gradient at Cathedral Hill, some of the transect push core sediments resided within zones of active catagenesis (Fig. 2; Dalzell et al., 2021). The degradation rates of each TEX₈₆ lipid were independently measured for the four push cores (Eq. 2; Fig. S2). As the abundance of both CLs and IPLs differentially decreases through the various core sediment profiles with turnover rates that appear to be constrained by porewater temperature changes (section 3.1), the degradation rates must also record the effects of thermochemical oxidative weathering (Fig. 3B). In this case, ϕ and θ are treated as grouped parameters. To determine if individual lipid classes were selectively removed during degradation, the variance (s^2) of the rate change as measured from its respective regression slope (i.e. $m_{\log k}$) from the TEX₈₆ lipids (Figure S2; Table S4 from Eq. 2) were calculated. For the Cathedral Hill transect, the calculated $m_{\log k}$ s^2 is 0.20, which is due to accelerated degradation rates for higher ring lipids, GDGT-3 and Cren', in samples from cores 1 and 2, where high vent temperatures resulted in hydrocarbon generation of the sediments (Dalzell et al., 2021). A weighing function for the degree of lipid class selectivity during turnover is proposed:

$$\phi + \theta = 1 / {}_M\text{TEX}_{86}^{0.2} \quad (6)$$

When applied to Eq. 4, the corrected data series produces an average transect $_{SS+WC}\text{TEX}_{86}^H$ reconstructed SST of 23.66 ± 0.59 °C with a near-zero partial least squares regression slope (Table 2; Figure 6B). As these modeled values are within the 23–24 °C obtained for the 21-year (1982–2004) satellite-derived MASST data for the Guaymas Basin region (Herrera-Cervantes et al., 2007). Based on these calculations, nearly all ${}_M\text{TEX}_{86}$ attenuation can be attributed to sediment microbial overprinting coupled to diagenetic and catagenetic loss of lipids consistent with prior observations at Guaymas Basin (Schouten et al., 2003; Zhang et al., 2011). The high degree of influence this has on the TEX₈₆ proxy is striking given that the upper water flux of GDGTs at Cathedral Hill is estimated to represents up to 93% of the total intact polar and core GDGT lipid pool within these sediments. In this regard, this study demonstrates the benthic microbial community can influence TEX₈₆ measurements.



598
599
600
601 **FIGURE 6.** Reconstructed combined $_{SS}TEX_{86}$ and SSTs $_{WC}TEX_{86}$ from Eq. 4 (A) with and (B) without ϕ ,
602 K , and θ scaling parameters compared to measured porewater temperatures. Red, green, blue, and brown
603 circles indicate recorded values from cores 1, 2, 3, and 4, respectively. $_{M}TEX_{86}$ values are plotted for
604 reference (open black diamonds). Yellow field is the 23–24 °C range observed for the 21-year (1982–2004)
605 satellite-derived MASST data (Herrera-Cervantes et al., 2007).

Table 2. Reconstructed sea surface temperatures.

Sample	Depth (cmbsf)	Porewater Temp. (°C)	<i>t</i> Time (yrs.)	<i>M</i> TEX ₈₆ (Measured <i>i</i> GDGT TEX ₈₆)	TEX ₈₆ ^H Reconstructed SST (°C)	TEX ₈₆ 1G- & 2G- GDGT IPLs (µg g ⁻¹)	Cumulative 1G- & 2G- GDGTs Loading with Depth (µg g ⁻¹)	<i>Sed</i> TEX ₈₆ (i.e. 1G- & 2G-GDGT IPLTEX ₈₆)	<i>c</i> (<i>d</i> _{0-n}) Cumulative Weighted IPL Loading (Eq. 5)
Core 1 (0-2cm)	1	19	10	0.56	21.2	4.80	0	0.58	0.00
Core 1 (2-4cm)	3	67	20	0.58	22.6	3.41	4.80	0.58	0.04
Core 1 (4-6cm)	5	85	30	0.58	22.3	1.29	8.21	0.55	0.07
Core 1 (6-8cm)	7	105	40	0.58	22.2	1.14	9.50	0.57	0.08
Core 1 (8-10cm)	9	117	50	0.59	22.9	1.41	10.64	0.72	0.09
Core 1 (10-12cm)	11	125	60	0.57	21.8	0.76	12.05	0.70	0.10
Core 1 (12-15cm)	13	135	70	0.61	23.8	0.72	12.81	0.69	0.11
Core 1 (15-18cm)	17	145	80	0.61	23.9	0.00	13.53	0.69*	0.11*
Core 1 (18-21cm)	20	153	90	0.63	24.9	0.00	13.53	0.69*	0.11*
Avg.				0.59	22.84				
Std. Dev.				0.02	1.16				
Core 2 (0-2cm)	1	11	10	0.55	20.6	4.33	0	0.49	0.00
Core 2 (2-4cm)	3	22	20	0.54	20.4	1.80	4.33	0.57	0.04
Core 2 (4-6cm)	5	20	30	0.54	20.5	0.76	6.13	0.60	0.05
Core 2 (6-8cm)	7	47	40	0.56	21.5	1.31	6.89	0.73	0.06
Core 2 (8-10cm)	9	60	50	0.58	22.3	0.88	8.20	0.70	0.07
Core 2 (10-12cm)	11	73	60	0.57	22.0	0.92	9.08	0.68	0.08
Core 2 (12-15cm)	13	87	70	0.57	21.8	0.40	10.00	0.73	0.08
Core 2 (15-18cm)	17	105	80	0.58	22.6	0.00	10.40	0.73*	0.09
Core 2 (18-21cm)	20	125	90	0.59	22.7	0.00	10.40	0.73*	0.09*
Avg.				0.56	21.61				
Std. Dev.				0.02	0.91				
Core 3 (0-2cm)	1	3.2	10	0.54	20.2	3.51	0	0.56	0.03
Core 3 (2-4cm)	3	8	20	0.53	19.9	1.79	3.51	0.51	0.01
Core 3 (4-6cm)	5	15	30	0.53	19.9	1.45	5.30	0.57	0.01
Core 3 (6-8cm)	7	26	40	0.54	20.3	1.77	6.74	0.55	0.01
Core 3 (8-10cm)	9	34	50	0.53	19.9	1.70	8.51	0.61	0.01
Core 3 (10-12cm)	11	43	60	0.54	20.3	2.16	10.21	0.71	0.02
Core 3 (12-15cm)	13	54	70	0.56	21.4	2.52	12.37	0.69	0.02
Core 3 (15-18cm)	17	66	80	0.55	20.9	4.72	14.89	0.73	0.04
Core 3 (18-21cm)	20	80	90	0.57	21.6	2.10	19.61	0.65	0.02
Avg.				0.54	20.50				
Std. Dev.				0.01	0.67				
Core 4 (0-2cm)	1	2	10	0.54	20.4	2.43	0	0.54	0.02
Core 4 (2-4cm)	3	8	20	0.53	20.0	1.75	2.43	0.44	0.01
Core 4 (4-6cm)	5	16	30	0.54	20.2	2.15	4.18	0.49	0.02

Core 4 (6-8cm)	7	18	40	0.52	19.3	1.76	6.34	0.47	0.01
Core 4 (8-10cm)	9	21	50	0.53	19.9	0.44	8.09	-	-
Core 4 (10-12cm)	11	23	60	0.53	19.8	2.20	8.54	-	-
Core 4 (12-15cm)	13	25	70	0.53	19.7	0.00	10.74	-	-
Avg.				0.53	19.90				
Std. Dev.				0.01	0.34				
Cumulative Avg.					19.68				
Cumulative Std. Dev.					0.79				

* Marks inherited values from the above sediment horizon.

Table 2. Reconstructed sea surface temperatures (continued).

Sample	Eq. 4 excluding $\phi+\theta+K$			Eq. 4 including $\phi+\theta+K$		
	$SS+WC\text{TEX}_{86} (M\text{TEX}_{86} - c(d_{0-n}) *_{Sed}\text{TEX}_{86})$	$SS+WC\text{TEX}_{86}^H$ (after Kim et al., 2010)	$SS+WC\text{TEX}_{86}^H$ Reconstructed SST ($^{\circ}\text{C}$)	$\phi+\theta$ (Eq. 6) (where $s^2 = 0.20$; Table S4)	$SS+WC\text{TEX}_{86}$	$SS+WC\text{TEX}_{86}^H$ Reconstructed SST ($^{\circ}\text{C}$) (after Kim et al., 2010)
Core 1 (0-2cm)	0.56	-0.25	21.2	1.12	0.63	24.7
Core 1 (2-4cm)	0.56	-0.25	21.4	1.12	0.63	24.9
Core 1 (4-6cm)	0.54	-0.27	20.3	1.13	0.62	24.2
Core 1 (6-8cm)	0.53	-0.27	19.8	1.13	0.61	23.9
Core 1 (8-10cm)	0.52	-0.28	19.5	1.14	0.61	23.7
Core 1 (10-12cm)	0.50	-0.30	17.9	1.15	0.58	22.6
Core 1 (12-15cm)	0.53	-0.27	20.0	1.13	0.62	24.2
Core 1 (15-18cm)	0.53	-0.27	19.8	1.13	0.61	24.1
Core 1 (18-21cm)	0.55	-0.26	21.0	1.13	0.63	25.0
Avg.	0.54	-0.27	20.10	1.13	0.61	24.14
Std. Dev.	0.02	0.02	1.08	0.01	0.02	0.75
Core 2 (0-2cm)	0.55	-0.26	20.6	1.13	0.62	24.2
Core 2 (2-4cm)	0.52	-0.28	19.2	1.14	0.60	23.3
Core 2 (4-6cm)	0.51	-0.29	18.7	1.14	0.59	22.9
Core 2 (6-8cm)	0.52	-0.28	19.3	1.14	0.60	23.4
Core 2 (8-10cm)	0.53	-0.28	19.7	1.14	0.61	23.8
Core 2 (10-12cm)	0.52	-0.28	19.1	1.14	0.60	23.4
Core 2 (12-15cm)	0.51	-0.29	18.5	1.14	0.59	23.0
Core 2 (15-18cm)	0.52	-0.28	19.2	1.14	0.60	23.5
Core 2 (18-21cm)	0.52	-0.28	19.3	1.14	0.60	23.6
Avg.	0.52	-0.28	19.32	1.14	0.60	23.47
Std. Dev.	0.01	0.01	0.60	0.00	0.01	0.40
Core 3 (0-2cm)	0.52	-0.28	19.4	1.14	0.60	23.3
Core 3 (2-4cm)	0.52	-0.28	19.4	1.14	0.60	23.3
Core 3 (4-6cm)	0.53	-0.28	19.5	1.14	0.60	23.4
Core 3 (6-8cm)	0.53	-0.27	19.9	1.13	0.60	23.6
Core 3 (8-10cm)	0.52	-0.28	19.4	1.14	0.60	23.3
Core 3 (10-12cm)	0.53	-0.28	19.6	1.14	0.60	23.5
Core 3 (12-15cm)	0.55	-0.26	20.7	1.13	0.62	24.3
Core 3 (15-18cm)	0.52	-0.28	19.3	1.14	0.60	23.4
Core3 (18-21cm)	0.55	-0.26	21.0	1.13	0.62	24.6
Avg.	0.53	-0.27	19.79	1.14	0.60	23.64
Std. Dev.	0.01	0.01	0.62	0.00	0.01	0.49
Core 4 (0-2cm)	0.53	-0.27	19.8	1.13	0.60	23.6
Core 4 (2-4cm)	0.53	-0.28	19.7	1.14	0.60	23.4

Core 4 (4-6cm)	0.53	-0.28	19.8	1.14	0.60	23.5
Core 4 (6-8cm)	0.52	-0.29	19.0	1.14	0.59	22.9
Core 4 (8-10cm)	-	-	-	-	-	-
Core 4 (10-12cm)	-	-	-	-	-	-
Core 4 (12-15cm)	-	-	-	-	-	-
Avg.	0.53	-0.28	19.51	1.07	0.60	23.38
Std. Dev.	0.01	0.01	0.38	0.00	0.01	0.31
Cumulative Avg.			19.68			23.66
Cumulative Std. Dev.			0.79			0.59

608

609

610

611 **4. Conclusions**

612 In this study, we demonstrate a pronounce overprint of *c*GDGTs sourced from the ocean floor sedimentary
613 archaeal community at the Cathedral Hill vent site in Guaymas Basin. The overprint is marked by lipids
614 with more cyclized ring moieties marking an adaptive response by archaea to rigidify the cellular
615 membranes against localized heat stress. This in turn has resulted in the commonly used TEX₈₆
616 paleoclimate proxy to partially record advecting porewaters temperatures. As the vast majority of *c*GDGTs
617 in these sediments is sourced from the overlying water column, the impact on the TEX₈₆ ratio is further the
618 product of rapid lipid turnover rates and diagenetic and catagenetic alteration processes potentially unique
619 to the hydrothermal system. Together, these factors resulted in absolute TEX₈₆^H temperature offsets of up to
620 4 °C based on calibrations closely suited to the latitudinal position of Guaymas Basin. To untangle the
621 impact of these coupled drivers on the TEX₈₆ proxy, we further present a method to correct the overprints
622 by both the water column and subsurface archaeal community using IPLs extracted from both of these
623 sources. Although, we have not been able to test this model with lipid inputs from the overlying water
624 column, we have demonstrated its effectiveness at removing sediment sourced overprints, which may not be
625 unique to hydrothermal systems. This approach should be capable of being extended to all near-surface
626 marine sediment systems and may improve the quality of calibration models or climate reconstructions that
627 are based on modern TEX₈₆ measures.

628

629

630 **Conflicts of Interest**

631 The authors declare no conflict of interest.

632

633 **Supplementary information**

634 Supplementary material related to this article can be found on-line at <https://doi.org/.....>

635 **References**

636 Bentley, J. N., Ventura, G. T., Dalzell, C. J., Walters, C. C., Peters, C. A., Mennito, A. S., Nelson, R. K.,
637 Reddy, C. M., Walters, C. J., Seewald, J., & Sievert, S. M. (2022). Archaeal lipid diversity, alteration,
638 preservation at Cathedral Hill, Guaymas Basin, and its link to the deep time preservation paradox.
639 Organic Geochemistry. 163:104302. doi.org/10.1016/j.orggeochem.2021.104302.
640
641 Besseling, M., Hopmans, E. C., Koenen, M., van der Meer, M. T. J., Vreugdenhil, S., Schouten, S.,
642 Sinninghe Damsté, J. S., & Villanueva, L. (2019). Depth-related differences in archaeal populations
643 impact the isoprenoid tetraether lipid composition of the Mediterranean Sea water column. Organic
644 Geochemistry, 135, 16–31. doi.org/10.1016/j.orggeochem.2019.06.008.

645 Besseling, M. A., Hopmans, E. C., Bale, N. J., Schouten, S., Sinninghe Damsté, J. S., & Villanueva, L.
646 (2020). The absence of intact polar lipid-derived GDGTs in marine waters dominated by Marine
647 Group II: Implications for lipid biosynthesis in Archaea. *Sci Rep* 10, 294. doi.org/10.1038/s41598-
648 019-57035-0.

649 Biddle, J. F., Cardman, Z., Mendlovitz, H., Albert, D. B., Lloyd, K. G., Boetius, A., & Teske, A. (2012).
650 Anaerobic oxidation of methane at different temperature regimes in Guaymas Basin hydrothermal
651 sediments. *The ISME Journal* 6, 1018–1031. doi.org/10.1038/ismej.2011.164.

652 Boetius, A., Ravensschlag, K., Schubert, C., Rickert, D., Widdel, F., Gieseke, A., Amann, R., Jørgensen,
653 B.B, Witte, U., & Pfannkuche, O. (2000). A marine microbial consortium apparently mediating
654 anaerobic oxidation of methane. *Nature* 407, 623–626. https://doi.org/10.1038/35036572.

655 Boyd, E., Hamilton, T., Wang, J., He, L., & Zhang, C. (2013). The role of tetraether lipid composition in
656 the adaptation of thermophilic archaea to acidity. *Frontiers in Microbiology*, 4, 62.

657 Brochier- Armanet, C., Boussau, B., Gribaldo, S., & Forterre, P. (2008). Mesophilic Crenarchaeota:
658 proposal for a third archaeal phylum, the Thaumarchaeota. *National Review Microbiology* 6, 245–
659 252. doi:10.1038/nrmicro1852.

660 Carr, S. A., Schubotz, F., Dunbar, R. B., Mills, C. T., Dias, R., Summons, R. E., & Mandernack, K. W.
661 (2018). Acetoclastic Methanosaeta are dominant methanogens in organic-rich Antarctic marine
662 sediments. *The ISME Journal*, 12(2), 330–342. https://doi.org/10.1038/ismej.2017.150.

663 Curray, J. R., Moore, D. G., Lawver, L. A., Emmel, F. J., Raitt, R. W., Henry, M., & Kieckhefer, R. (1979).
664 Tectonics of the Andaman Sea and Burma: convergent margins. In J.S. Watkins, L. Montadert, P.W.
665 Dickerson (Eds.) *Geological and Geophysical Investigations of Continental Margins*, AAPG Memoir
666 29, 189–198.

667 Dalzell, C. J., Ventura, G. T., Nelson, R. K., Reddy, C. M., Walters, C. J., Seewald, J., & Sievert, S. M.
668 (2021). Resolution of multi-molecular hydrocarbon transformation in petroleum-bearing sediments
669 from the Cathedral Hill hydrothermal vent complex at Guaymas Basin, Gulf of California by
670 comprehensive two-dimensional gas chromatography and chemometric analyses. *Organic*
671 *Geochemistry*, 152, 104173.

672 De Rosa, M., & Gambacorta, A. (1988). The lipids of archaebacteria. *Progress in lipid research*, 27, 153–
673 175.

674 Elling, F.J., Könneke, M., Lipp, J.S., Becker, K.W., Gagen, E.J., & Hinrichs, K.-U. (2014). Effects of
675 growth phase on the membrane lipid composition of the thaumarchaeon *Nitrosopumilus maritimus*
676 and their implications for archaeal lipid distributions in the marine environment. *Geochimica et*
677 *Cosmochimica Acta*, 141, 579–597.

678 Elling, F. J., Könneke, M., Mußmann, M., Greve, A., & Hinrichs, K. U. (2015). Influence of temperature,
679 pH, and salinity on membrane lipid composition and TEX₈₆ of marine planktonic thaumarchaeal
680 isolates. *Geochimica et Cosmochimica Acta*, 171, 238–255.

681 Gieskes, J. M., Simoneit, B. R., Brown, T., Shaw, T. J., Wang, Y. C., & Magenheimer, A. (1988).
682 Hydrothermal fluids and petroleum in surface sediments of Guaymas Basin, Gulf of California: a case
683 study. *The Canadian Mineralogist*, 26, 589–602.

684 Gliozzi, A., Paoli, G., De Rosa, M., & Gambacorta, A. (1983). Effect of isoprenoid cyclization on the
685 transition temperature of lipids in thermophilic archaebacteria. *Biochimica et Biophysica Acta (BBA)-*
686 *Biomembranes*, 735, 234–242.

700 Herrera-Cervantes, H.; Lluch-Cota, D. B., Lluch-Cota, S. E., & Gutiérrez-de-Velasco, S. G. (2007). The
701 ENSO signature in sea-surface temperature in the Gulf of California. *Journal of Marine Research*, 65,
702 589–605. doi.org/10.1357/002224007783649529.

703

704 Herfort, L., Schouten, S., Boon, J. P. & Sinninghe Damsté, J. S. (2006). Application of the TEX₈₆
705 temperature proxy to the southern North Sea. *Organic Geochemistry* 37, 1715–26.

706

707 Ho, S. L. & Laepple, T. (2016). Flat meridional temperature gradient in the early Eocene in the subsurface
708 rather than surface ocean. *Nature Geoscience*, 9, 606–610.

709

710 Hollis, C.J., Taylor, K.W.R., Handley, L., Pancost, R.D., Huber, M., Creech, J.B., Hines, B.R., Crouch,
711 E.M., Morgans, H.E.G., Crampton, J.S., Gibbs, S., Pearson, P.N., & Zachos, J.C. (2012). Early
712 Paleogene temperature history of the Southwest Pacific Ocean: Reconciling proxies and models. *Earth*
713 *and Planetary Science Letters* 349–350, 53–66

714

715 Hopmans, E. C., Weijers, J. W., Schefuß, E., Herfort, L., Sinninghe Damsté, J. S., & Schouten, S. (2004). A
716 novel proxy for terrestrial organic matter in sediments based on branched and isoprenoid tetraether
717 lipids. *Earth and Planetary Science Letters*, 224, 107–116.

718

719 Huguet, C., Cartes, J. E., Sinninghe Damsté, J. S., & Schouten, S. (2006). Marine crenarchaeotal membrane
720 lipids in decapods: Implications for the TEX₈₆ paleothermometer. *Geochemistry, Geophysics,*
721 *Geosystems*, 7. doi 10.1029/2006GC001305.

722

723 Huguet, C., Martrat, B., Grimalt, J. O., Sinninghe Damsté, J. S. & Schouten, S. (2011). Coherent millennial-
724 scale patterns in U37 k0 and TEX₈₆ H temperature records during the penultimate interglacial-to-
725 glacial cycle in the western Mediterranean. *Paleoceanography* 26. DOI: 10.1029/2010PA002048.

726

727 Huguet, C., Schimmelmann, A., Thunell, R., Lourens, L. J., Sinninghe Damsté, J. S., & Schouten, S.
728 (2007). A study of the TEX₈₆ paleothermometer in the water column and sediments of the Santa
729 Barbara Basin, California. *Paleoceanography*, 22. doi 10.1029/2006PA001310.

730

731 Hurley, S.J., Elling, F.J., Könneke, M., Buchwald, C., Wankel, S.D., Santoro, A.E., Lipp, J.S., Hinrichs, K.-
732 U., Pearson, A. (2016). Influence of ammonia oxidation rate on thaumarchaeal lipid composition and
733 the TEX₈₆ temperature proxy. *Proceedings of the National Academy of Sciences, U. S. A.* 113, 7762–
734 7767.

735

736 Kallmeyer, J., & Boetius, A. (2004). Effects of temperature and pressure on sulfate reduction and anaerobic
737 oxidation of methane in hydrothermal sediments of Guaymas Basin. *Applied and Environmental*
738 *Microbiology*. 70, 1231–1233. doi.org/10.1128/AEM.70.2.1231-1233.2004.

739

740 Karner, M. B., DeLong, E. F., Karl, D. M. (2001). Archaeal dominance in the mesopelagic zone of the
741 Pacific Ocean. *Nature*. 25, 409(6819), 507–510. doi: 10.1038/35054051.

742

743 Kashefi, K., & Lovley, D. R. (2003). Extending the upper temperature limit for life. *Science*, 301, 934–934.

744

745 Kim, J. H., Schouten, S., Hopmans, E. C., Donner, B., & Damsté, J. S. S. (2008). Global sediment core-top
746 calibration of the TEX₈₆ paleothermometer in the ocean. *Geochimica et Cosmochimica Acta*, 72,
747 1154–1173.

748

749 Kim, J. H., Van der Meer, J., Schouten, S., Helmke, P., Willmott, V., Sangiorgi, F., Koç, N., Hopmans, E.
750 C. & Damsté, J. S. S. (2010). New indices and calibrations derived from the distribution of
751 crenarchaeal isoprenoid tetraether lipids: Implications for past sea surface temperature
752 reconstructions. *Geochimica et Cosmochimica Acta*, 74, 4639–4654.

753

Kim J.-H., Romero O. E., Lohmann G., Donner B., Laepple T., Haam E. & Sinninghe Damsté J. S. (2012a) Pronounced subsurface cooling of North Atlantic waters off Northwest Africa during Dansgaard-Oeschger interstadials. *Earth and Planetary Science Letters*, 339–340, 95–102.

Kim, J. H., Crosta, X., Willmott, V., Renssen, H., Bonnin, J., Helmke, P., Schouten, S. & Sinninghe Damsté, J. S. (2012b). Holocene subsurface temperature variability in the eastern Antarctic continental margin. *Geophysical Research Letters*, 39. doi 10.1029/2012GL051157.

Kim J.-H., Schouten, S., Rodrigo-Gamiz, M., Rampen, S., Marino, G., Huguët, C., Helmke, P., Buscail, R., Hopmans, E. C., Pross, J., Sangiorgi, F., Middelburg, J. B. M., & Sinninghe Damsté J. S. (2015). Influence of deep-water derived isoprenoid tetraether lipids on the paleothermometer in the Mediterranean Sea. *Geochimica et Cosmochimica Acta*, 150, 125–141.

Knappy, C. S., Chong, J. P., & Keely, B. J. (2009). Rapid discrimination of archaeal tetraether lipid cores by liquid chromatography-tandem mass spectrometry. *Journal of the American Society for Mass Spectrometry*, 20, 51–59.

Lawrence, K. T., Pearson, A., Castaneda, I. S., Ladow, C., Peterson, L. C., Lawrence, G. E. (2020). Comparison of Late Neogene U^{k}_{37} and TEX_{86} Paleotemperature records from the eastern equatorial Pacific at orbital resolution. *Paleoceanography and Paleoclimatology*, 35, 1–16.

Lengger, S.K., Hopmans, E.C., Reichart, G.-J., Nierop, K.G.J., Sinninghe Damsté, J.S., Schouten, S. (2012). Intact polar and core glycerol dibiphytanyl glycerol tetraether lipids in the Arabian Sea oxygen minimum zone. Part II: Selective preservation and degradation in sediments and consequences for the TEX_{86} . *Geochimica et Cosmochimica Acta* 98, 244–258.

Lengger, S, K, Hopmans, E. C., Sinninghe Damsté, J. S., Schouten, S. (2014). Fossilization and degradation of archaeal intact polar tetraether lipids in deeply buried marine sediments (Peru Margin). *Geobiology*, 12(3), 212–220, <https://doi.org/10.1111/gbi.12081>.

Lincoln, S. A., Wai, B., Eppley, J. M., Church, M. J., Summons, R. E., & DeLong, E. F. (2014). Planktonic euryarchaeota are a significant source of archaeal tetraether lipids in the ocean. *Proceedings of the National Academy of Sciences, U. S. A.* 111, 9858–9863. doi: 10.1073/pnas.1409439111.

Lipp, J. S., & Hinrichs, K. U. (2009). Structural diversity and fate of intact polar lipids in marine sediments. *Geochimica et Cosmochimica Acta*, 73, 6816–6833.

Lipp, J. S., Morono, Y., Inagaki, F., & Hinrichs, K. U. (2008). Significant contribution of Archaea to extant biomass in marine subsurface sediments. *Nature*, 454, 991–994.

Liu, X. L., Leider, A., Gillespie, A., Gröger, J., Versteegh, G. J., & Hinrichs, K. U. (2010). Identification of polar lipid precursors of the ubiquitous branched GDGT orphan lipids in a peat bog in Northern Germany. *Organic Geochemistry*, 41, 653–660.

Liu, X. -L., Lipp, J. S., Hinrichs, K. -U. (2011). Distribution of core and intact GDGTs in marine sediments. *Organic Geochemistry* 42, 368–375.

Liu, X. L., Russell, D. A., Bonfio, C., Summons, R. E. (2018) Glycerol configurations of environmental GDGTs investigated using a selective $sn2$ ether cleavage protocol. *Organic Geochemistry*, 128, 57–62.

Lopes dos Santos R. A., Prange M., Castaneda I. S., Schefuß E., Mulitza S., Schulz M., Niedermeyer E. M., Sinninghe Damsté J. S. and Schouten S. (2010). Glacial–interglacial variability in Atlantic meridional overturning circulation and thermocline adjustments in the tropical North Atlantic. *Earth and Planetary Science Letters*, 300, 407–414.

810 Lunt, D. J., Haywood, A. M., Schmidt, G. A., Salzmann, U., Valdes, P. J., Dowsett, H. J., & Loptson, C.A.
811 (2012). On the causes of mid-Pliocene warmth and polar amplification. *Earth and Planetary Science*
812 *Letters*, 321-322, 128–138, doi:10.1016/j.epsl.2011.12.042.
813

814 Ma, C., Coffinet, S., Lipp, J. S., Hinrichs, K. U., & Zhang, C. (2020). Marine Group II Euryarchaeota
815 Contribute to the Archaeal Lipid Pool in Northwestern Pacific Ocean Surface Waters. *Frontiers in*
816 *microbiology*, 11, 1034. <https://doi.org/10.3389/fmicb.2020.01034>.
817

818 Macalady, J. L., Vestling, M. M., Baumler, D., Boekelheide, N., Kaspar, C. W., & Banfield, J. F. (2004).
819 Tetraether-linked membrane monolayers in *Ferroplasma* spp: a key to survival in
820 acid. *Extremophiles*, 8, 411–419.
821

822 McClymont, E. L., Ganeshram, R. S., Pichevin, L. E., Talbot, H. M., van Dongen, B. E., Thunell, R. C.,
823 Haywood, A.M., Singarayer, J.S. & Valdes, P. J. (2012). Sea-surface temperature records of
824 Termination 1 in the Gulf of California: Challenges for seasonal and interannual analogues of tropical
825 Pacific climate change. *Paleoceanography*, 27. doi 10.1029/2011PA002226.
826

827 McKay, L. J., MacGregor, B. J., Biddle, J. F., Albert, D. B., Mendlovitz, H. P., Hoer, D. R., Lipp, J.S.,
828 Lloyd, K.G & Teske, A. P. (2012). Spatial heterogeneity and underlying geochemistry of
829 phylogenetically diverse orange and white Beggiatoa mats in Guaymas Basin hydrothermal
830 sediments. *Deep Sea Research Part I: Oceanographic Research Papers*, 67, 21–31.
831

832 Meyer, S., Wegener, G., Lloyd, K. G., Teske, A., Boetius, A., & Ramette, A. (2013). Microbial habitat
833 connectivity across spatial scales and hydrothermal temperature gradients at Guaymas
834 Basin. *Frontiers in Microbiology*, 4, 207.
835

836 Naafs, B. D. A., Rohrssen, M., Inglis, G. N., Lahteenoja, O., Feakins, S. J., Collinson, M. E., Kennedy,
837 E.M., Singh, P.K., Singh, M.P., Lunt, D.J., & Pancost, R. D. (2018). High temperatures in the
838 terrestrial mid-latitudes during the early Palaeogene. *Nature Geoscience*, 11, 766–771.
839

840 O'Brien, C.L., Robinson, S.A. Pancost, R.D., Sinninghe Damste, J.S., Schouten, S., Lunt, D.J., Alsenz, H.,
841 Bomemann, A., Bottini, C., Brassell, S.C., Farnsworth, A., Forster, A., Huber, B.T., Inglis, G.N.,
842 Jenkyns, H.C., Linnert, C., Littler, K., Markwick, P., McAnena, A., Mutterlose, J., Naafs, B.D.A.,
843 Puttmann, W., Sluijs, A., van Helmond, N.A.G.M., Vellekoop, J., Wagner, T., & Wrobel, N.E.
844 (2017). Cretaceous sea-surface temperature evolution: Constraints from TEX₈₆ and planktonic
845 foraminiferal oxygen isotopes. *Earth-Science Reviews*. 172, 224–247.
846

847 Pearson, A. & Ingalls, A. E. (2013) Assessing the use of archaeal lipids as marine environmental proxies.
848 *Annual Review Earth Planetary Science*. 41, 15.1–15.26.
849

850 Pearson, A., Huang, Z., Ingalls, A. E., Romanek, C. S., Wiegand, J., Freeman, K. H., Smittenberg, R. H. &
851 Zhang, C. L. (2004). Nonmarine crenarchaeol in Nevada hot springs. *Applied and Environmental*
852 *Microbiology*, 70, 5229–5237.
853

854 Petrick, B., Reuning, L., & Martinez-Garcia (2019) Distribution of Glycerol Dialkyl Glycerol Tetraethers
855 (GDGTs) in Microbial Mats From Holocene and Miocene Sabkha Sediments. *Frontiers in Earth*
856 *Science*. 04. doi.org/10.3389/feart.2019.00310.
857

858

859 Qin, W., Carlson, L. T., Armbrust, E. V., Devol, A. H., Moffett, J. W., Stahl, D. A., & Ingalls, A. E. (2015).
860 Confounding effects of oxygen and temperature on the TEX₈₆ signature of marine Thaumarchaeota.
861 *Proceedings of the National Academy of Sciences, U. S. A.* 112(35), 10,979–10,984.
862 doi.org/10.1073/pnas.1501568112.
863

864 Robinson, S. A., Ruhl, M., Astley, D. L., Naafs, B. D. A., Farnsworth, A. J., Bown, P. R., Jenkyns, H. C.,
865 Lunt, D. J., O'Brien, C., Pancost, R. D., & Markwick, P. J. (2017). Early Jurassic North Atlantic sea-
866 surface temperatures from TEX₈₆. *Palaeothermometry. Sedimentology*, 64, 215–230.
867
868 Rommerskirchen, F., Condon, T., Mollenhauer, G., Dupont, L. M., & Schefuß, E. (2011). Miocene to
869 Pliocene development of surface and subsurface temperatures in the Benguela Current system.
870 *Paleoceanography*, 26, PA3216, 1-15. doi.org/10.1029/2010PA002074.
871
872 Schouten, S., Hopmans, E. C., & Sinninghe Damsté, J. S. (2013). The organic geochemistry of glycerol
873 dialkyl glycerol tetraether lipids: A review. *Organic Geochemistry*, 54, 19–61.
874
875 Schouten, S., Hopmans, E. C., & Sinninghe Damsté, J. S. (2004). The effect of maturity and depositional
876 redox conditions on archaeal tetraether lipid palaeothermometry. *Organic Geochemistry*, 35, 567–571.
877
878 Schouten, S., Hopmans, E. C., Schefuß, E., & Sinninghe Damsté, J. S. (2002). Distributional variations in
879 marine crenarchaeotal membrane lipids: a new tool for reconstructing ancient sea water
880 temperatures? *Earth and Planetary Science Letters*, 204, 265–274.
881
882 Schouten S., Wakeham S. G., Hopmans E. C. and Sinninghe Damsté J. S. (2003) Biogeochemical Evidence
883 that Thermophilic Archaea Mediate the Anaerobic Oxidation of Methane. *Appl. Environ. Microbiol.*
884 69, 1680-1686.
885
886 Seki, O., Bendle, J. A., Haranda, N., Kobayashi, M., Sawada, K., Moossen, H., Inglis, G. N., Nagao, S., &
887 Sakamoto, T. (2014). Assessment and calibration of TEX₈₆ paleothermometry in the Sea of Okhotsk
888 and sub-polar North Pacific region: Implications for paleoceanography. *Progress in Oceanography*.
889 126, 254–266.
890
891 Sinninghe Damsté J. S., Rijpstra W. I. C., Hopmans E. C., den Uijl M. J., Weijers J. W. H. and Schouten S.
892 (2018) The enigmatic structure of the crenarchaeol isomer. *Organic Geochemistry* 124, 22-28.
893
894 Stadnitskaia, A., Nadezhkin, D., Abbas, B., Blinova, V., Ivanov, M. K., & Sinninghe Damsté, J. S. (2008).
895 Carbonate formation by anaerobic oxidation of methane: evidence from lipid biomarker and fossil
896 16S rDNA. *Geochimica et Cosmochimica Acta*, 72(7), 1824–1836.
897
898 Sturt, H. F., Summons, R. E., Smith, K., Elvert, M., & Hinrichs, K. U. (2004). Intact polar membrane lipids
899 in prokaryotes and sediments deciphered by high-performance liquid chromatography/electrospray
900 ionization multistage mass spectrometry—new biomarkers for biogeochemistry and microbial
901 ecology. *Rapid communications in mass spectrometry*, 18, 617–628.
902
903 Teske, A., Callaghan, A. V., & LaRowe, D. E. (2014). Biosphere frontiers of subsurface life in the
904 sedimented hydrothermal system of Guaymas Basin. *Frontiers in Microbiology*, 5, 362.
905
906 Teske, A., De Beer, D., McKay, L. J., Tivey, M. K., Biddle, J. F., Hoer, D., Lloyd, K.G., Lever, M.A., Røy,
907 H., Albert, D.B & MacGregor, B. J. (2016). The Guaymas Basin hiking guide to hydrothermal
908 mounds, chimneys, and microbial mats: Complex seafloor expressions of subsurface hydrothermal
909 circulation. *Frontiers in Microbiology*, 7, 75.
910
911 Tierney, J. E. (2014). Biomarker-based inferences of past climate: the TEX₈₆ paleotemperature proxy. In
912 H.D. Holland & K.K. Turekian (Eds.) *Treatise on Geochemistry* (2nd Ed.) 12, 379-939.
913
914 Uda, I., Sugai, A., Itoh, Y. H., & Itoh, T. (2001). Variation in molecular species of polar lipids from
915 *Thermoplasma acidophilum* depends on growth temperature. *Lipids*, 36, 103–105.
916
917 Umoh, U., Li L., Luckge, A., Schwartz-Schampera, U., & Naafs, D. (2020). Influence of hydrothermal vent
918 activity on GDGT pool in marine sediments might be less than previously thought. *Organic*
919 *Geochemistry*. 104102. doi.org/10.1016/j.orggeochem.2020.104102.

920
 921 Wakeham, S. G., Lewis, C. M., Hopmans, E. C., Schouten, S., & Sinninghe Damsté, J. S. (2003). Archaea
 922 mediate anaerobic oxidation of methane in deep euxinic waters of the Black Sea. *Geochimica et*
 923 *Cosmochimica Acta*, 67, 1359–1374.
 924
 925 Wang, J. X., Wei, Y., Wang, P., Hong, Y., & Zhang, C. L. (2015). Unusually low TEX₈₆ values in the
 926 transitional zone between Pearl River estuary and coastal South China Sea: impact of changing
 927 archaeal community composition. *Chemical Geology*, 402, 18–29. doi:
 928 10.1016/j.chemgeo.2015.03.002.
 929
 930 Weijers, J. W., Schefuß, E., Kim, J. H., Sinninghe Damsté, J. S., & Schouten, S. (2014). Constraints on the
 931 sources of branched tetraether membrane lipids in distal marine sediments. *Organic Geochemistry*, 72,
 932 14–22.
 933
 934 Weijers, J. W., Schouten, S., van den Donker, J. C., Hopmans, E. C., & Sinninghe Damsté, J. S. (2007).
 935 Environmental controls on bacterial tetraether membrane lipid distribution in soils. *Geochimica et*
 936 *Cosmochimica Acta*, 71, 703–713.
 937
 938 Wuchter, C., Schouten, S., Wakeham, S. G., & Sinninghe Damsté, J. S. (2005). Temporal and spatial
 939 variation in tetraether membrane lipids of marine Crenarchaeota in particulate organic matter:
 940 Implications for TEX₈₆ paleothermometry. *Paleoceanography*, 20, doi 10.1029/2004PA001110.
 941
 942 Wuchter, C., Schouten, S., Wakeham, S. G. & Sinninghe Damsté, J. S. (2006). Archaeal tetraether
 943 membrane lipid fluxes in the northeastern Pacific and the Arabian Sea: implications for TEX₈₆
 944 paleothermometry. *Paleoceanography* 21.
 945
 946 Xie, S., Lipp, J.S., Wegener, G., Ferdelman, T.G., Hinrichs, K-U. (2013). Turnover of microbial lipids in
 947 the deep biosphere and growth of benthic archaeal populations. *Proceedings of the National Academy*
 948 *of Sciences, U. S. A.* 110, 6010–6014.
 949
 950 Yoshinaga, M. Y., Kellermann, M. Y., Rossel, P. E., Schubotz, F., Lipp, J. S., & Hinrichs, K. U. (2011).
 951 Systematic fragmentation patterns of archaeal intact polar lipids by high-performance liquid
 952 chromatography/electrospray ionization ion-trap mass spectrometry. *Rapid Communications in Mass*
 953 *Spectrometry*, 25, 3563–3574.
 954
 955 Zeng, Z., Liu, X. L., Farley, K. R., Wei, J. H., Metcalf, W. W., Summons, R. E., & Zhang, Y. G., Pagani,
 956 M., & Wang, Z. (2016). Ring Index: A new strategy to evaluate the integrity of TEX₈₆
 957 paleothermometry. *Paleoceanography*, 31, 220–232.
 958
 959 Zhang, Y. G., Zhang, C. L., Liu, X. L., Li, L., Hinrichs, K. U., & Noakes, J. E. (2011). Methane Index: A
 960 tetraether archaeal lipid biomarker indicator for detecting the instability of marine gas hydrates. *Earth*
 961 *and Planetary Science Letters*, 307, 525–534.
 962
 963 Zhang, Y. G., Pagani, M. & Wang, Z. (2016). Ring Index: A new strategy to evaluate the integrity of
 964 TEX₈₆ paleothermometry. *Paleoceanography and Paleoclimatology* 31:220–232, doi.org/
 965 10.1002/2015PA002848.
 966
 967 Zhu, C., Lipp, J. S., Wörmer, L., Becker, K. W., Schröder, J., & Hinrichs, K. U. (2013). Comprehensive
 968 glycerol ether lipid fingerprints through a novel reversed phase liquid chromatography-mass
 969 spectrometry protocol. *Organic Geochemistry*, 65, 53–62.